Neuron
Article

Coupled Oscillations Mediate Directed Interactions between Prefrontal Cortex and Hippocampus of the Neonatal Rat

Marco D. Brockmann,[1,2] Beatrice Pöschel,[1,2] Nicole Cichon,[1,2] and Ileana L. Hanganu-Opatz[1,*]
[1]Developmental Neurophysiology, Center for Molecular Neurobiology, University Medical Center Hamburg-Eppendorf, 20251 Hamburg, Germany
[2]These authors contributed equally to this work
*Correspondence: hangop@zmnh.uni-hamburg.de
DOI 10.1016/j.neuron.2011.05.041

SUMMARY

The coactivation of prefrontal and hippocampal networks in oscillatory rhythms is critical for precise information flow in mnemonic and executive tasks, yet the mechanisms governing its development are still unknown. Here, we demonstrate that already in neonatal rats, patterns of discontinuous oscillatory activity precisely entrain the firing of prefrontal neurons and have distinct spatial and temporal organization over cingulate and prelimbic cortices. Moreover, we show that hippocampal theta bursts drive the generation of neonatal prefrontal oscillations by phase-locking the neuronal firing via axonal pathways. Consequently, functional impairment of the hippocampus reduces the prefrontal activity. With ongoing maturation continuous theta-gamma oscillations emerge and mutually entrain the prejuvenile prefrontal-hippocampal networks. Thus, theta-modulated communication within developing prefrontal-hippocampal networks may be relevant for circuitry refinement and maturation of functional units underlying information storage at adulthood.

INTRODUCTION

Brain processing during executive and mnemonic tasks relies on interactions within complex neuronal networks (Buzsáki and Draguhn, 2004; Womelsdorf et al., 2007). Generally, information processing within local networks is globally integrated (Buzsáki, 2006), yet the maturation and the underlying mechanisms of this efficient cortical computation are still poorly elucidated. The relevance of information integration between neuronal networks for higher cognitive abilities is exemplary illustrated in the case of the prefrontal cortex (PFC) and hippocampus (Hipp). The PFC is involved in gating of memory, attention, and decision making (Miller, 2000; Vertes, 2006). It receives strong monosynaptic glutamatergic inputs from the CA1 area and subiculum of the Hipp (Swanson, 1981; Thierry et al., 2000). Simultaneous recordings from the PFC and Hipp demonstrated that hippocampal theta oscillations modulate the firing of prefrontal neurons, thereby delivering the temporal coordination of both oscillating neuronal networks and enabling information transfer and storage (Siapas and Wilson, 1998; Sirota et al., 2008; Wierzynski et al., 2009). Consequently, the prefrontal-hippocampal oscillatory coactivation may provide the mechanisms for organizing and consolidating memory traces (Euston et al., 2007; Hyman et al., 2010).

Coupling of neuronal networks in oscillatory rhythms is not a hallmark of the adult brain, but rather emerges early during development. However, the highly discontinuous and fragmented temporal organization of the activity patterns in immature networks remarkably differs from the adult one (Dreyfus-Brisac, 1962; Vecchierini et al., 2007; Vanhatalo and Kaila, 2006). These bursts of activity alternating with ''silent'' interburst intervals have been characterized in primary sensory cortices (visual cortex, barrel cortex). In these areas they synchronize and integrate inter- and intracortical networks and seem to act as an early functional template of later emerging cortical topography (Hanganu et al., 2006; Huberman et al., 2006; Yang et al., 2009). Correlated bursts of activity have been identified also in the neonatal Hipp, where diverse patterns of activity (sharp waves, theta and gamma oscillations, ripples) start to emerge during the first postnatal week (Lahtinen et al., 2002; Mohns and Blumberg, 2010). It has been proposed that these immature hippocampal patterns of activity are a prerequisite for the maturation of hippocampal circuitry (Mohns and Blumberg, 2008).

Despite recent significant progress in understanding the mechanisms of prefrontal-hippocampal coactivation that underlies information transfer and storage in the adult brain, key questions concerning the maturation of functional communication between these two areas and its anatomical substrate remain open. When and how do patterns of oscillatory activity start to synchronize the developing prefrontal networks? Anatomical studies revealed that the PFC reaches the adult cytoarchitecture and connectivity not before adolescence, corresponding to the delayed maturation of executive and mnemonic abilities when compared to sensory and motor skills (Van Eden and Uylings, 1985). Is the emergence of coordinated patterns of activity in the PFC consequently delayed? Does the early emerging hippocampal activity contribute to the generation of prefrontal oscillations and how do the interactions between these two areas evolve during postnatal development to enable adequate information processing and storage at adulthood?

To address these questions, we recorded unit activity and local field potentials from the PFC and Hipp in neonatal and prejuvenile rats in vivo. We characterize here for the first time the oscillatory coupling and the spike-timing relationships between the PFC and Hipp throughout early postnatal development.

RESULTS

The PFC Shows Complex Patterns of Oscillatory Activity during the First Two Postnatal Weeks

We examined the activity patterns in the medial PFC by performing extracellular recordings of the local field potential (FP) and multiple unit activity (MUA) in neonatal and prejuvenile (postnatal day [P] 0–14) urethane-anesthetized rats (n = 104 pups) in vivo (Figure 1; see Table S1 available online). In contrast to the rat primary visual (V1) and somatosensory (S1) cortices (Khazipov et al., 2004; Hanganu et al., 2006; Yang et al., 2009) expressing discontinuous patterns of oscillatory activity already at birth, the PFC develops such patterns starting with P3 and no coordinated activity was present in P0–2 pups (n = 11) (Figure S1). These initial intermittent spindle-shaped field oscillations (Figures 1B and Ci) showed similar properties with the previously described spindle bursts (SB) in the V1 and S1 of neonatal rats. When recorded from multiple recording sites covering the entire PFC, SB had a relative short duration (1.86 ± 0.02 s, n = 4717 bursts from 27 pups) and small amplitude (123.56 ± 1.19 μV). In contrast to the V1 and S1 activity, the prefrontal SB occurred rarely (1.11 ± 0.14 bursts/min) and their main frequency was slower, ranging within theta frequency band (7.8 ± 0.05 Hz).

Starting with P5 short episodes (0.2 ± 0.003 s, n = 1951 events from 19 pups) of low gamma-band (37.08 ± 0.15 Hz) oscillations overlaid spindle-shaped oscillations with main frequency of 9.2 ± 0.11 Hz and large amplitudes (251.61 ± 2.82 μV). Due to the tight connection between the superimposed gamma oscillations and the slow theta-alpha bursts, we defined this pattern of prefrontal activity as nested gamma spindle bursts (NG) (Figures 1B, 1Cii, and 1Ciii). They occurred at a frequency of 0.67 ± 0.09 bursts/min, lasted 2.12 ± 0.03 s and were accompanied (Figure 1Ciii) or not (Figure 1Cii) by MUA. Although the main difference between SB and NG was the presence of superimposed gamma episodes, the two patterns of prefrontal activity have also distinct properties (Figure S2). Similar to early urethane-independent oscillations in the primary sensory cortices prefrontal SB and NG were marginally modified by progressive reduction of the urethane dose from 1 to 0.125 g/kg body weight (n = 16 pups). Their occurrence and main frequency remained constant, whereas their amplitude decreased from 145 ± 7 μV to 107.7 ± 5.8 μV for SB and from 277.7 ± 10.1 μV to 160 ± 8 μV for NG.

With ongoing maturation the properties of SB and NG modified significantly. Their occurrence, duration, amplitude, and dominant frequency gradually increased with age (Figure 1E). Around P10–11 the PFC switched from discontinuous SB and NG to continuous oscillatory rhythms (Figures 1D and S4), suggesting that the neuronal networks generating oscillatory patterns underwent a substantial process of reorganization. The continuous rhythm with main frequency in theta-band (6.11 ± 0.03 Hz, n = 19 pups) and amplitudes ranging from 56 to 544 μV expressed superimposed short episodes of gamma activity (Figure 1D). The amplitude and the dominant frequency of continuous oscillatory activity in the PFC were relatively stable during the second postnatal week (Figure 1E).

These results indicate that corresponding to the previously reported delayed anatomical maturation of the PFC, network activity emerges here later than in the V1 or S1 of age-matched rat pups. The presence of discontinuous and later of continuous theta-gamma rhythms mirrors early complex intra- and intercortical interactions.

Oscillatory Entrainment of Neuronal Firing within the Neonatal PFC

To gain a first insight into the network interactions leading to the generation of oscillatory patterns in the neonatal PFC we analyzed the relationship between neuronal discharge and SB/NG (Figure 2A). The mean firing rate during the whole recording was very low (0.67 ± 0.11 Hz, n = 7 pups), MUA predominantly accompanying the prefrontal oscillations. Only a low fraction of oscillation-associated spikes (15.7% ± 2.1%, n = 2479 spikes from 6 pups) was organized in bursts. When calculating separately the firing rate for SB and NG, a significantly ($p < 0.001$) higher spike discharge was associated with NG (14.77 ± 1 Hz, n = 7 pups) than with SB (3.5 ± 0.42 Hz, n = 7 pups) and was mainly confined to their gamma episodes (42.29 ± 1.83 Hz) (Figure 2B). However, the majority (77% ± 17%) of nested gamma episodes were not associated with MUA discharge (Figure 1Cii versus 1Ciii). When occurring together, gamma episodes and MUA were tightly coupled and a prominent peak in their cross-correlogram emerged 30 to 50 ms after the onset of gamma episodes (Figure 2C). The prominent increase in the firing rate during gamma episodes was preceded by an ~50 ms long period of low MUA, during which the occurrence probability of gamma episodes was also very low. Examination of spike-gamma phase relationship showed that 12 out of 13 prefrontal neurons (n = 10 pups) fired shortly after the trough of gamma cycle (Figure 2D). This gamma phase-locking of prefrontal neurons suggests that the gamma episodes time the firing of the neonatal PFC. Moreover, the entrainment of local networks in gamma rhythms occurred not randomly, but timed by the underlying slow rhythm of NG (NG cycle). The gamma episodes occur with the highest probability shortly before the trough of the NG cycle (Figure 2E).

These results indicate that complex mechanisms control the neuronal firing in the neonatal PFC. The prefrontal neurons fire phase-locked to the nested gamma episodes that are, in turn, clocked by the underlying slow rhythm of NG.

Distinct Prefrontal Areas Show Different Spatial Organization of Early Oscillatory Patterns

According to their location and cytoarchitecture several subareas can be functionally distinguished within the PFC as early as P6 (Van Eden and Uylings, 1985). Multielectrode recordings were performed simultaneously in the dorsally located anterior cingulate cortex (Cg) as well as in the subjacent prelimbic cortex (PL) to characterize the spatial organization of the network activity over the developing PFC. Although SB and NG were

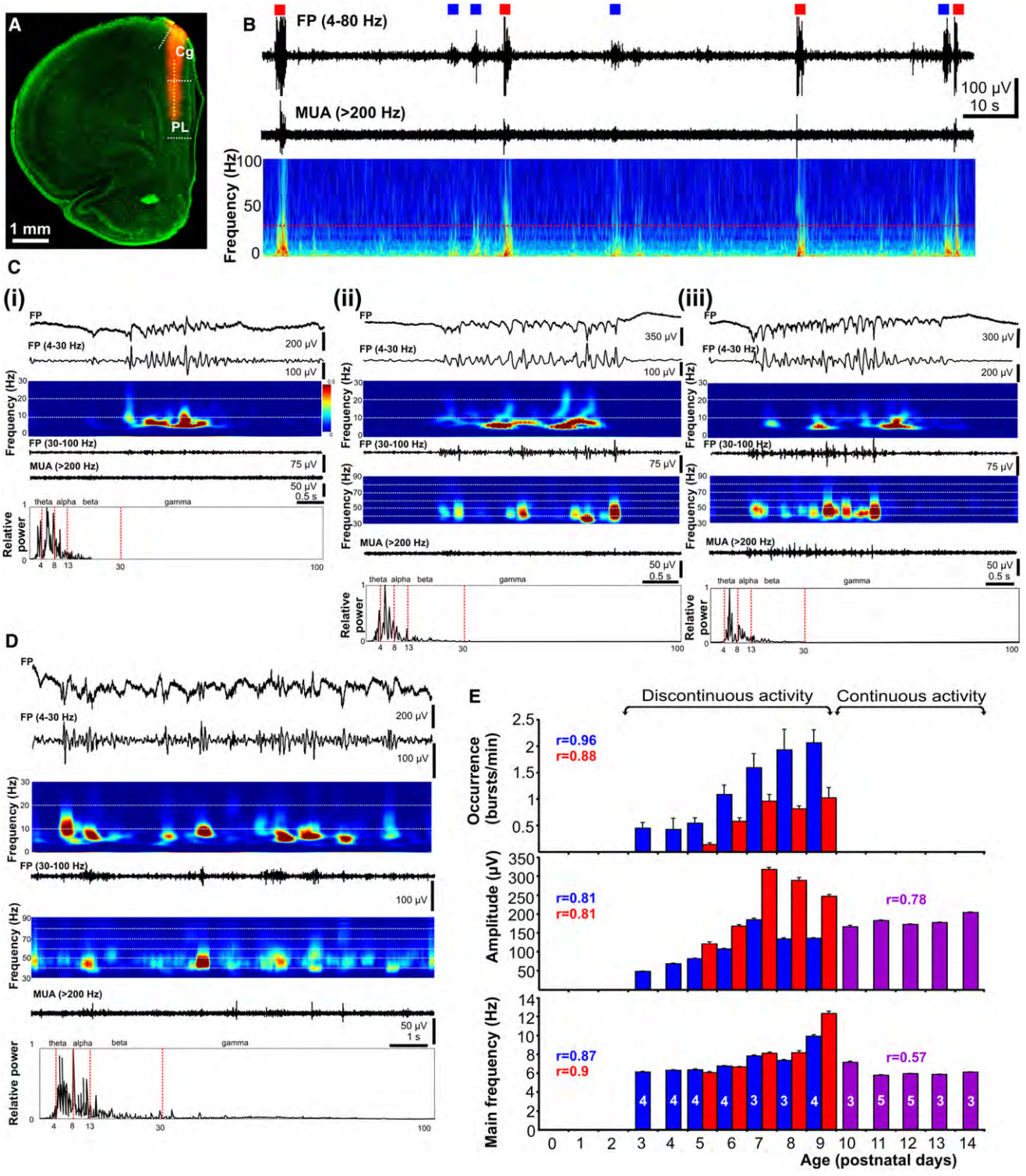

Figure 1. Patterns of Oscillatory Activity in the Rat PFC In Vivo during the First Two Postnatal Weeks

(A) Digital photomontage reconstructing the location of the DiI-labeled recording electrode (orange) in the PFC of a Nissl-stained 100 μm thick coronal section (green) from a P6 rat. Yellow dots mark the 16 recording sites covering the Cg and PL.

(B) Extracellular FP recording of the intermittent oscillatory activity in the PFC from a P7 rat (top) and the corresponding MUA after 200 Hz high-pass filtering (below). Blue squares mark the SB, whereas red squares correspond to NG. Traces are accompanied by the "whitened" spectrogram of FP at identical time scale. The red dotted line marks the lower border of gamma frequency band (30 Hz).

present in both regions, their occurrence significantly differed between the Cg and PL (Figure 3A; Table S2). In the Cg, SB represented the dominant pattern of activity, very few NG being present in this area. In contrast, NG are the dominant pattern of prelimbic activity. Moreover, the duration, main frequency, power, and frequency distribution of SB as well as the amplitude and power of NG showed significant differences in the Cg and PL (Table S2).

Beside different properties, SB and NG showed also distinct current generators over the Cg and PL as indicated by the current source density (CSD) analysis performed on 38 SB and 69 NG from 5 pups (Figure 3B). The most common CSD profile for SB present in 43.05% ± 11.7% of events was a narrow source-sink pair confined to the upper cingulate area. In contrast, the majority of NG (72.03% ± 7.34%) showed a prominent sink within the PL.

In the majority of recordings, neither SB nor NG were restricted to one channel but rather occurred simultaneously at several neighboring recording sites of the 4x4 array electrode (Figures 3C and 3D). To estimate the spatial organization of SB and NG over the Cg and PL, the cross-correlation and coherence at dominant frequency were assessed for all recording sites in relationship to one reference channel (n = 9 pups) (Figure 3C). The majority of cingulate SB appeared widely synchronized, whereas the relative low occurrence of NG precluded a consistent analysis of their coupling over the Cg. In the PL, most of SB (720 out of 1200) were also widely synchronized, while the majority of prelimbic NG (768 out of 1472) synchronized the upper layers and the cortical plate (CP) (Figure 3D). The distinct spatial organization, current generators, and synchronization patterns of SB and NG argue for different oscillatory entrainment of cingulate and prelimbic networks during neonatal development.

This distinction persisted also at prejuvenile age, since the amplitude and main frequency of continuous theta-gamma rhythms in P10–14 rats (n = 19) differed significantly between the Cg and PL. Moreover, the power of superimposed gamma episodes was significantly ($p < 0.001$) higher in the PL (2737 ± 109 μV^2/Hz, n = 19 pups) than in the Cg (2646 ± 110 μV^2/Hz). The distinct properties of discontinuous versus continuous prefrontal oscillations suggest that the networks entrained for their generation are subject of intense refinement and reorganization during postnatal development.

The Oscillatory Entrainment of Prefrontal-Hippocampal Networks Modifies during Development

In the light of the recently demonstrated function of hippocampal theta to temporally coordinate the prefrontal activity at adulthood (Siapas et al., 2005; Sirota et al., 2008) the question arises, when during development the hippocampal control over the PFC emerges. The premise for addressing this question was to characterize in neonatal and prejuvenile rats (n = 33) the activity of the CA1 area of the intermediate Hipp, which at adulthood is known to densely project to the PFC (Hoover and Vertes, 2007). Already at birth prominent sharp-waves (SPWs) (Table S3; Figure S3A), which reversed across the pyramidal layer (Str pyr) and were accompanied by strong MUA discharge (13.07 ± 3.51 Hz, n = 10 pups), were present in the CA1 area. From P1 on, discontinuous oscillations with main frequency in theta band (7.03 ± 0.15 Hz, n = 398 events from 15 pups) were additionally present (Table S3; Figure S3B). They represent the dominant pattern of slow oscillatory activity in the neonatal Hipp. Since their mechanisms of generation are still unknown and might differ from those of the adult theta rhythms, we defined these events as hippocampal theta bursts. About one-third of the theta bursts (136 out of 398 events) were accompanied by SPWs. Their duration and maximal amplitude were significantly ($p < 0.001$) higher than of the theta bursts without superimposed SPWs (Table S3). As previously reported (Palva et al., 2000; Lahtinen et al., 2002), gamma oscillations and ripples developed toward the end of the first postnatal week and appeared superimposed on theta bursts and SPWs, respectively. The gamma episodes appeared almost exclusively confined to the theta bursts (Figure S3Bii) and very few of them (16.35%, n = 104 events) were theta independent. In contrast to the prefrontal NG, the phase coupling between hippocampal theta and gamma is absent at this age (Figure S3Bii). As for the adult Hipp (Buzsáki et al., 1992; Le Van Quyen et al., 2008), the low amplitude (~25 μV) neonatal ripples appeared in conjunction with SPWs, are restricted to the Str pyr, and are tightly coupled to MUA discharge (Figure S3C). Similar to neocortical areas, hippocampal activity switched from discontinuous bursts to continuous theta rhythms during early postnatal development (n = 6 pups) (Figure S3D; Table S3). However, this transition occurred 1–2 days earlier in the Hipp than in the PFC (Figure S4) and may reflect the

(C) (i) Characteristic SB displayed before (top) and after band-pass (4–30 and 30–100 Hz) filtering (middle), and the corresponding MUA after 200 Hz high-pass filtering. Note the low spike discharge during SB. Color-coded frequency plot shows the wavelet spectrum of the FP at identical time scale. Fast Fourier transformation (FFT) of the FP illustrates the relative power of SB with maximal frequency at ~6 Hz (bottom). (ii) Characteristic NG displayed before (top) and after band-pass (4–30 and 30–100 Hz) filtering (middle), and the corresponding MUA after 200 Hz high-pass filtering. Note the presence of prominent gamma episodes that are not accompanied by spike discharge. The upper color-coded wavelet spectrum and the FFT reveal the main frequency of NG within theta-alpha band, whereas the nested gamma episodes appear as periodic high power spots on the bottom wavelet. (iii) Characteristic NG displayed before (top) and after band-pass (4–30 and 30–100 Hz) filtering (middle), and the corresponding MUA after 200 Hz high-pass filtering. Note the presence of prominent gamma episodes that are accompanied by strong spike discharge. The upper color-coded wavelet spectrum and the FFT reveal the main frequency of NG within theta-alpha band, whereas the nested gamma episodes appear as periodic high power spots on the bottom wavelet spectrum.
(D) Extracellular FP recording of the continuous oscillatory activity in the PFC from a P13 rat displayed before (top) and after band-pass (4–30 Hz and 30–100 Hz) filtering (middle) and the corresponding MUA after 200 Hz high-pass filtering. The upper color-coded wavelet spectrum and the FFT reveal the prominent activity below 10 Hz, whereas the bottom spectrum displays the power of gamma episodes superimposed on the continuous activity.
(E) Developmental profile of SB and NG as well as of continuous activity in the rat PFC during the first two postnatal weeks. Occurrence (top), amplitude (middle), and main frequency (bottom) of SB (blue), NG (red), and continuous activity (violet) were averaged and displayed as bar diagrams (mean ± SEM). The number of pups investigated for each age is marked on the bars. The properties of SB and NG were significantly dependent on age (ANOVA test). The coefficients (r) of linear regression analysis were marked in blue (SB), red (NG), and violet (continuous activity), respectively.
See also Figures S1 and S2 and Tables S1 and S2.

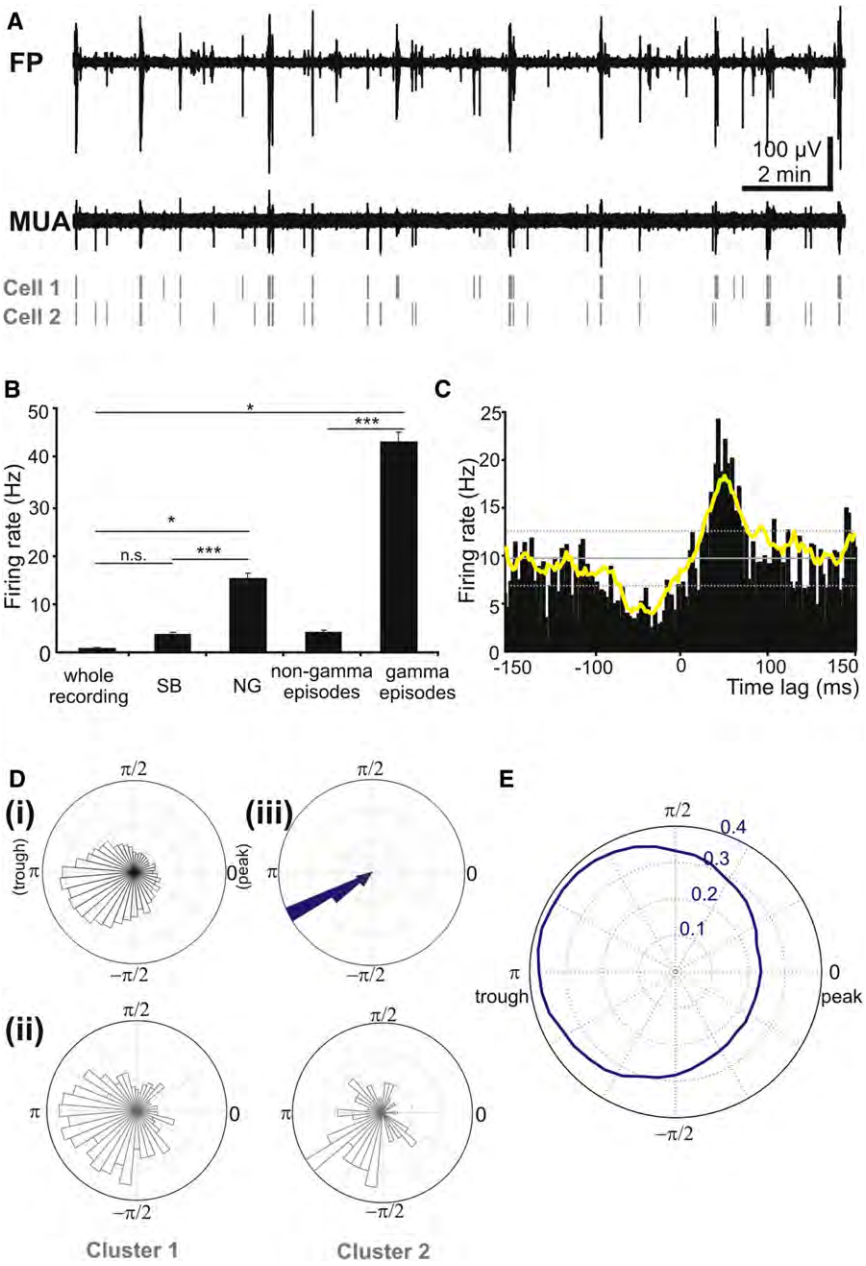

Figure 2. Timing Relationships among Neuronal Firing, Nested Gamma Episodes, and NG in the Neonatal PFC

(A) Extracellular FP recording (4–80 Hz) of intermittent oscillatory activity in the PFC of a P6 rat accompanied by corresponding MUA and rasters of single-unit activity (gray, 2 neurons) obtained after clustering.

(B) Relationship between the firing rate of prefrontal neurons and the different patterns of oscillatory activity in the neonatal PFC. Bar diagram (mean ± SEM) shows the high firing rate during the superimposed gamma episodes of NG and the low firing rate during SB and non-gamma episodes.

(C) Representative histogram correlating individual (black bars) or averaged (yellow line) MUA with the onset (time lag 0 ms) of gamma episodes. Note the confinement of increased firing within the gamma episode. The solid gray line corresponds to the mean firing rate, whereas the dashed gray lines mark the borders of confidence interval for $\alpha = 0.01$.

(D) (i) Polar histogram of the mean distribution of spikes on the gamma phase when averaged for all significantly phase-locked neurons (n = 12). (ii) Same for two clustered neurons (cluster 1 with 557 spikes, cluster 2 with 67 spikes). (iii) Polar histogram displaying the distribution of mean phase vectors for all significantly phase-locked neurons.

(E) Polar plot of the normalized probability of gamma occurrence over the NG cycle.

differences in the maturation of cytoarchitecture and connectivity (Angevine, 1975).

Several approaches were used to characterize the interactions between prefrontal and hippocampal activity during the first two postnatal weeks. First, we examined the temporal correspondence of discontinuous oscillations across the PFC and CA1 area of the intermediate Hipp in simultaneous recordings from both areas. The majority of hippocampal theta bursts occurred within a narrow time window (<3 s) with SB or NG in the Cg (87.7%, n = 203 events from 6 pups) or PL (93.6%, n = 296 events from 9 pups) (Figure 4A), their onset either preceding (Cg: 20.7% of events, delay 0.5 ± 0.006 s, PL: 13.9% of events, delay 1 ± 0.14 s), succeeding (Cg: 3.9% of events, delay 0.14 ± 0.05 s, PL: 3.4% of events, delay 0.63 ± 0.24 s) or matching (Cg: 63.1% of events, PL: 73.4% of events) the onset of prefrontal events. Second, the temporal synchrony between hippocampal and prefrontal activity was assessed by spectral coherence analysis (Figures 4B and S5A). Due to the predominance of distinct activity patterns with different spatial organization in the Cg and PL, we separately analyzed the cingulate-hippocampal and the prelimbic-hippocampal synchronization. Coherence coefficients for simultaneously occurring oscillations in the Cg and Hipp (0.52 ± 0.02, n = 59 events from 6 pups) as well as in the PL and Hipp (0.53 ± 0.02, n = 90 events from 9 pups) were relatively high. To decide whether the strong prefrontal-hippocampal coupling was restricted to simultaneously occurring oscillatory events, the coherence analysis was performed also for oscillations at shuffled time windows. The resulting coherence coefficients (Cg: 0.39 ± 0.02, n = 59 events from 6 pups, PL: 0.47 ± 0.002, n = 90 events from 9 pups) were significantly lower than for original time windows of oscillatory activity. To verify that this high level of coherence was a genuine feature of the prefrontal-hippocampal interactions, we additionally assessed the synchronization between the Hipp and V1 as well as between

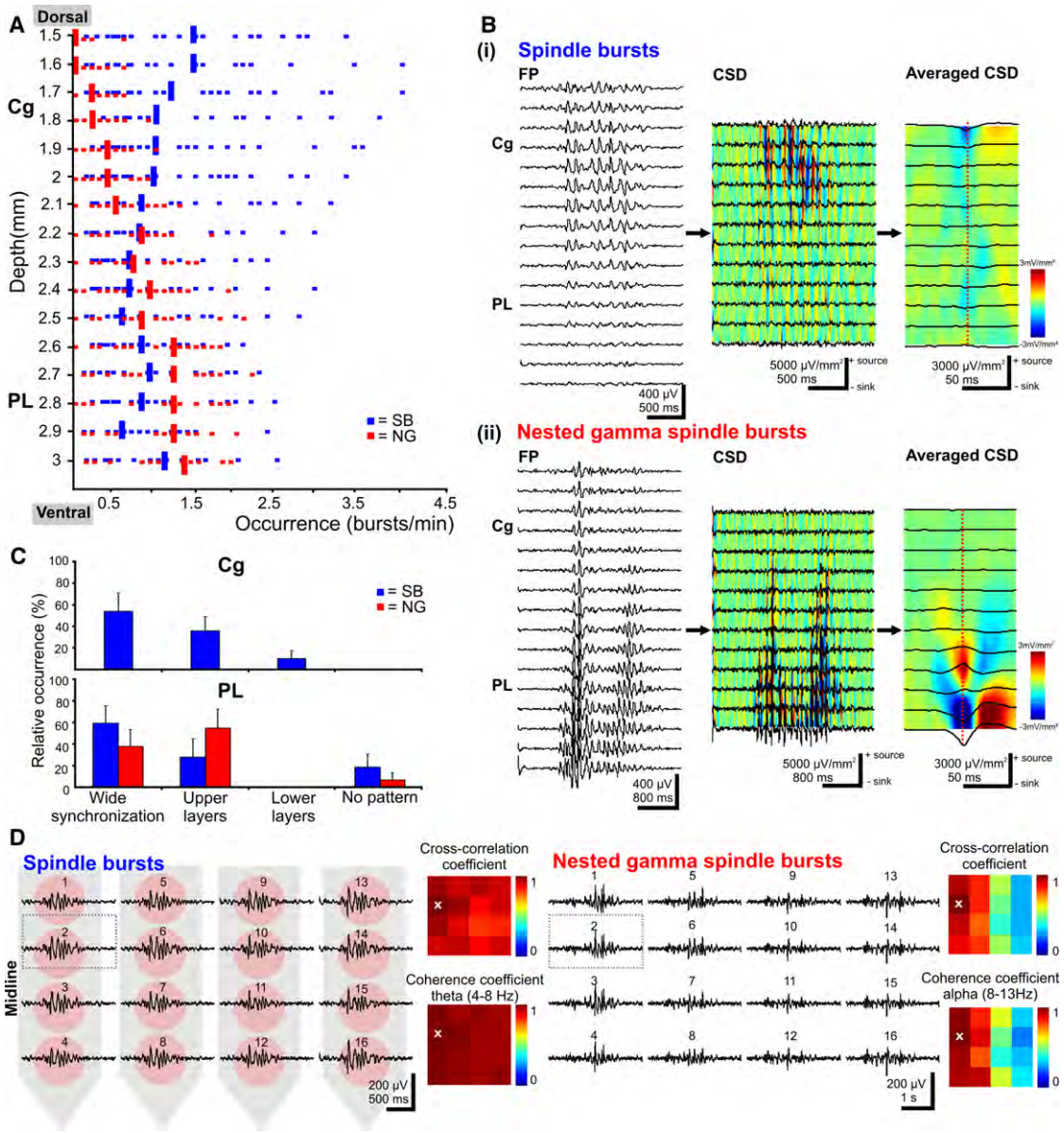

Figure 3. Spatial Organization of Early Oscillatory Patterns in the Neonatal PFC

(A) Distribution of SB (blue) and NG (red) recorded from 23 P5–9 pups over the entire PFC, including the Cg and PL. The occurrence of SB and NG was significantly different (ANOVA, $p < 0.01$ and $p < 0.001$) over the Cg and PL. Median values are marked by solid lines and each dot represents the value from one pup.

(B) Spatial distribution of current generators for SB (i) and NG (ii) in the Cg and PL of neonatal rat. Simultaneous FP recordings in the PFC of a P6 rat with 16-channel one shank Michigan electrode (interelectrode distance of 100 µm) (left) were displayed together with the corresponding CSD analysis (middle) and the averaged CSD plots (right) that were calculated for 33 troughs from 8 SB and 104 troughs from 14 NG. Note the prominent sink/source of NG in the PL.

(C) Bar diagram summarizing the relative occurrence of different patterns of intrahemispheric synchronization for SB (blue) and NG (red) in the Cg and PL. The displayed values were averaged (mean ± SEM) from 9 P5–9 pups. The low occurrence of NG in the Cg precluded a reliable analysis.

(D) Simultaneous FP recordings from the PL of a P6 rat with the 4 × 4-channels electrode array (interelectrode distance of 125 µm horizontally and 50 µm vertically) and the corresponding color-coded plots of maximal cross-correlation and coherence coefficients illustrating the wide (left) versus upper layer synchronization (right) for SB and NG, respectively. The channel with maximal amplitude was used as reference and is marked by gray dotted boxes over recording traces and by white X in plots.

different neocortical areas. The level of coherence for oscillatory events in the CA1 area and V1 was significantly ($p < 0.01$) lower (0.37 ± 0.02, n = 48 events from 3 pups) than for the prefrontal-hippocampal interactions (Figure S5B). Different levels of synchronization were observed over distinct neocortical areas. While the oscillations recorded at two adjacent sites in the PFC showed very high coherence coefficients (Cg: 0.98 ± 0.002, n = 59 events from 6 rats; PL: 0.96 ± 0.004, n = 90 from 9

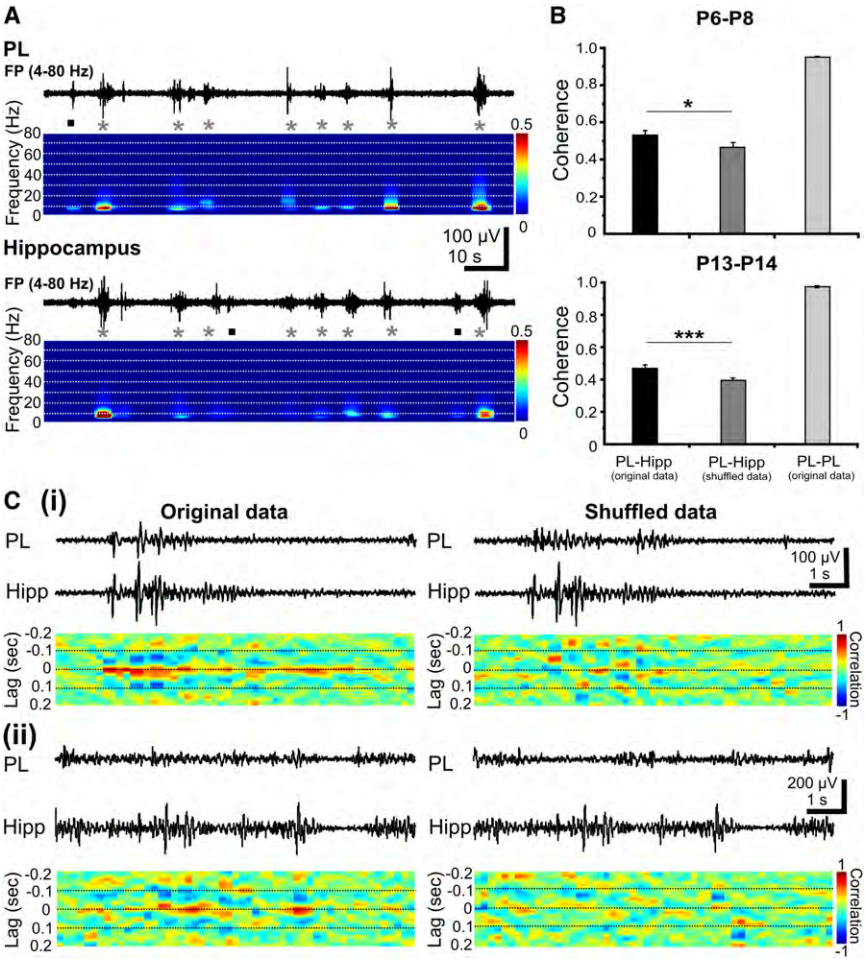

Figure 4. Dynamic Coupling of Hippocampal and Prefrontal Oscillatory Activity during Neonatal and Prejuvenile Development

(A) Simultaneous FP recordings of the discontinuous oscillatory activity in the PL and CA1 area of the intermediate Hipp accompanied by the color-coded wavelet spectra of the FP at identical time scale. Note the high incidence of simultaneously occurring (gray asterisks) hippocampal theta oscillations and prefrontal SB/NG as well as the presence of few events restricted to one area (black squares).

(B) Coherence of prelimbic-hippocampal oscillations calculated for discontinuous (top) and continuous (bottom) activity from 9 P6–8 pups and 7 P13–14 pups, respectively. Bar diagrams (mean ± SEM) reveal the significantly higher prelimbic-hippocampal coherence for original than for shuffled data (oscillatory events in the PL and Hipp occurring at different time points).

(C) Dynamics of prelimbic-hippocampal coupling. (i) Simultaneous FP recordings (4–80 Hz) of oscillatory activity in the PL and CA1 area of a P7 rat and the time-aligned sliding window cross-correlograms for original (left) and shuffled (right) data. Note the high and sustained correlation between the two regions through the oscillatory event. (ii) Same as (i) for continuous activity from a P13 rat where the peak correlation at time lag 0 ms vaxes and vanes. All other colors than green represent significant positive (red) or negative (blue) correlation.

See also Figures S3–S5 and Table S3.

pups) (Figures 4B and S5A), the prefrontal activity was not synchronized with the SB in the V1 or S1, since the calculated coherence coefficients were significantly ($p < 0.001$) smaller (Figure S5B). Therefore, nonspecific synchrony does not contribute to the prefrontal-hippocampal synchronization. A second artifactual source of high coherence between field oscillations of two areas may represent the conduction synchrony (Lachaux et al., 1999). Its contribution seems, however, to be very limited, since the coherence between prefrontal FP and hippocampal spikes, a measure of ''true synchrony'' due to neural coupling (Soteropoulos and Baker, 2006), was significantly ($p < 0.05$) higher than for shuffled data.

To investigate the dynamics of hippocampal-prefrontal coupling by oscillatory rhythms, we performed sliding window cross-correlation analysis of prefrontal SB/NG and hippocampal theta bursts (Figures 4Ci and S5Ci). The first peak of individual cross-correlation (~0 s lag) fluctuated systematically and periodically for both Cg-Hipp and PL-Hipp oscillations as sign of transient coupling and decoupling of the prefrontal and hippocampal regions. Remarkably, the coupling of the PL and Hipp in oscillatory bursts seems to be more stable than the coupling between the Cg and Hipp, since constantly high prefrontal-hippocampal cross-correlation during the entire burst was calculated for 25.2% of the prelimbic oscillations, but for only 9.5% of the cingulate bursts.

The synchronization of oscillatory rhythms in the PFC and Hipp persisted with ongoing maturation. Toward the end of the second postnatal week, the coherence coefficients calculated for continuous oscillatory discharge Cg-CA1 and PL-CA1 were similar to the values detected for discontinuous oscillations one week before (Cg: coherence 0.48 ± 0.02, n = 60 events from 6 pups; PL: coherence 0.46 ± 0.02, n = 70 events from 7 pups) (Figures 4B and S5A). However, the dynamics of prefrontal-hippocampal synchronization changed with age and only short lasting (~0.5 s) coupling followed by decoupling dominated the interactions between the Cg or PL and Hipp (Figures 4Cii and S5Cii).

Taken together, these results indicate that the prefrontal and hippocampal networks are coactivated in discontinuous or continuous oscillatory rhythms throughout early postnatal development.

Due to the symmetric interdependence of cross-correlation and coherence, they do not offer reliable insights into the direction of information flow between two brain areas. Therefore, the demonstrated temporary oscillatory coupling of the PL with the Hipp and to a lower extent of the Cg with the Hipp is a relationship

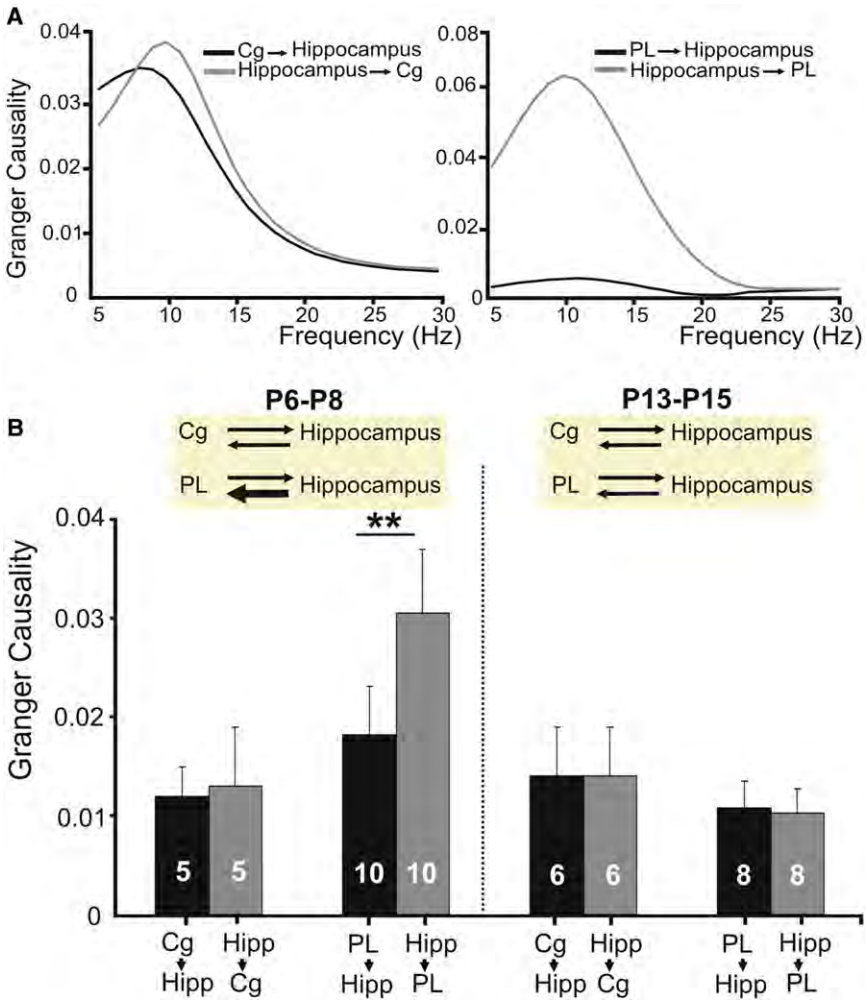

Figure 5. Directional Interactions between the PFC and Hipp during Postnatal Development

(A) Example of Granger causality spectra between the Cg and hippocampal CA1 area (left) and between the PL and CA1 area (right) for a P7 rat.

(B) Bar diagrams (mean ± SEM) displaying the mean Granger causality averaged over significant ($p < 0.05$) pairs of time segments for the interactions Cg-Hipp and PL-Hipp at the end of the first and the second postnatal week, respectively. The number of investigated pups is marked on bars. Insets, schematic representation of the causal relationships between prefrontal and hippocampal theta activity during both stages of development.

missing directionality. To estimate the causal strength of prefrontal-hippocampal interactions and its dynamics during development, Granger causality analysis, a powerful method for studying directed interactions between brain areas (Ding et al., 2000; Anderson et al., 2010), was carried out for pairs of signals in theta-frequency band from the PFC and Hipp. Whereas the peak Granger causality values from the neonatal Cg to the CA1, denoted as Cg → Hipp (n = 5 pups), were not significantly different from those in the opposite direction, denoted as Hipp → Cg (Figure 5), a different causal relationship was found for the interaction between the neonatal PL and Hipp. The hippocampal theta bursts drove stronger the prelimbic SB and NG than vice versa, since the peak Granger causality values were significantly higher for Hipp → PL than for the reciprocal connection PL → Hipp in all 10 investigated pups (Figure 5). The results are in line with the stable coupling between the PL and Hipp as revealed by coherence and cross-correlation analysis and support the driving role of hippocampal theta bursts for the prelimbic oscillations.

Toward the end of the second postnatal week the peak values of Granger causality for pairs of signals from the Cg or PL and Hipp were significant in all investigated pups (n = 14), but similar for both directions (Figure 5). Thus, we suggest that with progressive maturation, prefrontal and hippocampal networks mutually influence each other.

To identify the mechanisms underlying the directed communication between the developing PFC and Hipp, we assessed the spike-timing relationships between prefrontal neurons and hippocampal theta bursts as well as between pairs of neurons from the two areas. Due to the very low firing rate of cingulate neurons and the results of Granger causality analysis, we focused the investigation on the prelimbic neurons. For this, we performed acute multitetrode recordings from the PL and Hipp of P7–8 (n = 7 pups) and P13–14 (n = 5 pups) rats. In a first instance, we tested whether prelimbic neurons are phase-locked to the hippocampal theta bursts. The analysis revealed that ~9% of prelimbic neurons were significantly phase-locked to the hippocampal theta burst at both neonatal and prejuvenile age. In a second instance, we tested the impact of hippocampal firing on prelimbic cells and calculated the standardized cross-covariance ($Q_{i,j}$) between all pairs (i, j) of simultaneously recorded prelimbic and hippocampal neurons (52 prelimbic neurons and 59 hippocampal neurons in P7–8 rats, 201 prelimbic neurons and 63 hippocampal neurons in P13–14 rats). In neonatal rats, only few neurons (287 PL-Hipp pairs from 3 pups) had a firing rate exceeding the set threshold of 0.05 Hz and were used for further analysis. The cross-covariance computed for all prelimbic-hippocampal pairs revealed no consistent spike timing of prelimbic neurons relative to the hippocampal cells, but yielded to a rather broad peak centered at ~0 ms lag. However, when focusing only on the interactions between theta phase-locked prelimbic neurons and hippocampal cells (n = 30 pairs), we detected $Q_{i,j}$ peaks at positive time lags between 0 and 50 ms in 10% of cell pairs (Figure 6Aii). These data suggest that theta-locked prelimbic neurons fire immediately after the hippocampal neurons.

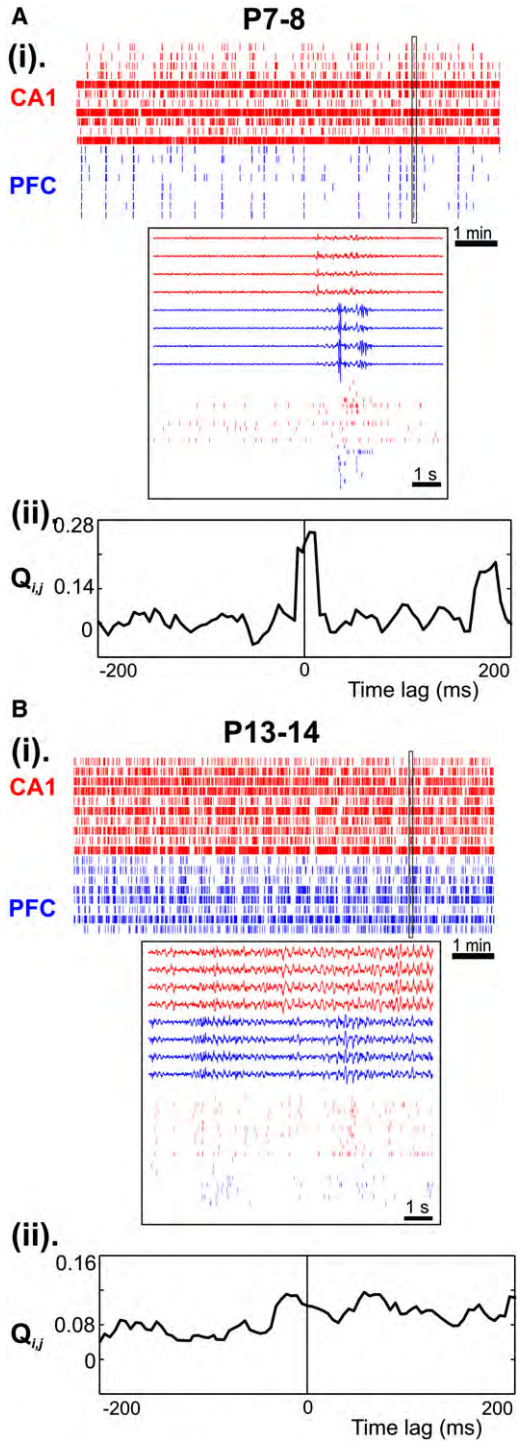

Figure 6. Spike-Timing Relationships between Prefrontal and Hippocampal Neurons in the Neonatal and Prejuvenile Rat

(A) (i) Spike trains from 11 CA1 (red) and 8 PL (blue) simultaneously recorded neurons from a P7 rat. Note the low firing rate of the immature prelimbic neurons. Inset, close-up of the spike trains shown in (A) displayed at enlarged time scale together with the corresponding FP on four prelimbic and four hippocampal recording sites of the multitetrode. (ii) Mean cross-covariance ($Q_{i,j}$) of all cell pairs including prelimbic neurons phase-locked to hippocampal theta. Only prefrontal-hippocampal pairs exceeding the significance level (α = 0.01) were considered for analysis (n = 23).

(B) (i) Same as (Ai) for 10 CA1 (red) and 8 PL neurons (blue) from a P13 rat. (ii) Same as (Aii) for all phase-locked prelimbic-hippocampal cells in prejuvenile rats (n = 63 pairs).

Toward the end of the second postnatal week the firing rate of prelimbic neurons significantly augmented, reducing the risk of spurious cross-covariance (Figure 6B versus 6A). In prejuvenile rats 99 out of 878 prelimbic-hippocampal cell pairs were used for further analysis after excluding neurons with firing rate <0.05 Hz. The spiking relationship between prelimbic and hippocampal cells changed, subsets of prelimbic neurons firing either before or after the hippocampal ones. Consequently, significant $Q_{i,j}$ detected in 63 pairs showed peak lags between −50 and 0 ms as well as between 0 and 100 ms (Figure 6Bii). The spike-timing relationship between prejuvenile prelimbic and hippocampal neurons confirms the theta-modulated mutual interactions between the two areas.

Axonal Projections Contribute to the Hippocampal Drive on Prefrontal Networks

The concept of Granger causality is statistical in nature and therefore, the causal influence of the Hipp on the PL does not imply that the hippocampal networks drive the prefrontal circuits by direct axonal pathways. More supportive of this hypothesis are the spike-timing relationships between prefrontal and hippocampal neurons ($Q_{i,j}$ peaks at max ± 100 ms time lag). While strong unidirectional and monosynaptic projections from intermediate/ventral Hipp innervate the adult PFC (Hoover and Vertes, 2007), no experimental findings document their ingrowth through postnatal development. To assess this issue, we injected bilaterally small amounts of the retrograde tracer Fluorogold (FG) into the PFC of P1 (n = 4) and P6 (n = 2) rat pups. The spreading of tracer over the entire neonatal PFC precluded reliable distinction between hippocampal innervation of the Cg and PL (Figures 7A and S6). Six to thirteen days after FG injection, labeled cells were found predominantly in the CA1 area of the intermediate and ventral Hipp, their number increasing until the end of the second postnatal week. Occasionally weaker staining of the CA3 area (n = 3 pups), subiculum (n = 4 pups), or dorsal Hipp (n = 1 pup) as well as of the entorhinal cortex (EC) (n = 5 pups) could be detected.

To identify the contribution of these direct hippocampal projections to the generation of oscillatory activity in the Cg and PL, the hippocampal CA1 area was electrically stimulated using a bipolar electrode (Figure S7A). Its insertion did not impair the cingulate or prelimbic oscillatory activity (n = 3 pups) (Figure S8). Single stimulation of the CA1 area evoked direct responses in the Cg and PL that started simultaneously after 12.2 ± 0.6 ms (n = 6 pups) and lasted 22.34 ± 1.71 ms and 23 ± 1.88 ms, respectively. In 3 out of 6 P7–9 rats the direct response was followed by network oscillations in 13.11% ± 4.7% of stimulations in the Cg and in 15.74% ± 4.75% of stimulations in the PL. The evoked SB started in the Cg 102 ± 10 ms and in the PL 103.1 ± 7.7 ms after the onset of stimulus (Figures 7B and 7C). Similar results were obtained when repetitive

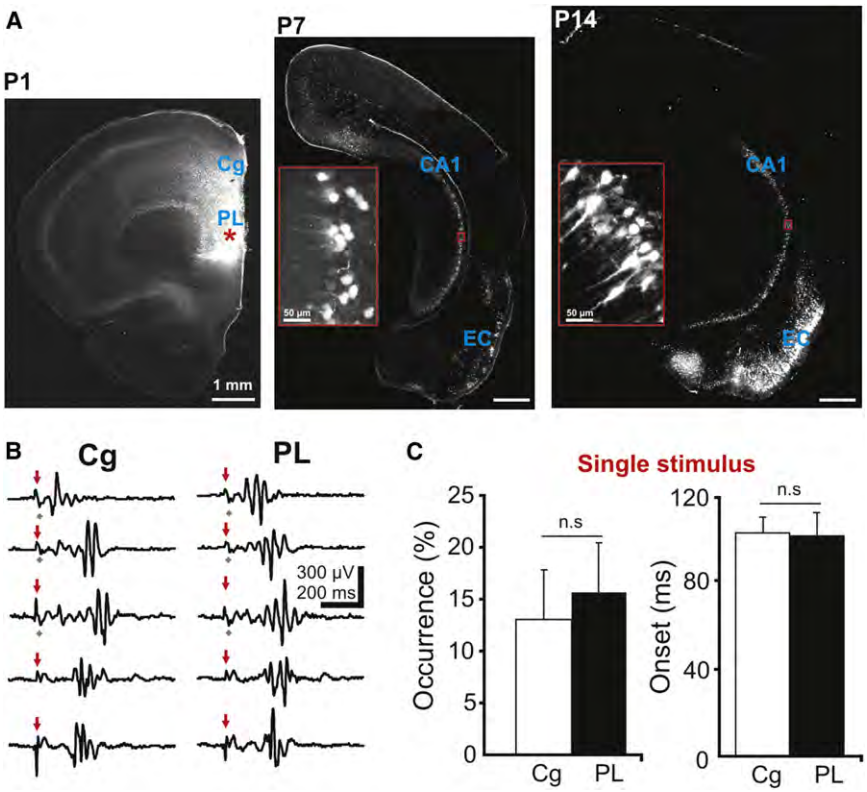

Figure 7. Role of Projections from the CA1 Area of the Intermediate Hipp to the Developing PFC for the Generation of Prefrontal Patterns of Activity

(A) Brightfield photomicrographs depicting retrogradely labeled neurons accumulating principally in the CA1 area and the EC of a P7 (middle) or a P14 (right) rat after FG injection (red star) in the PFC at P1 (left). Insets, retrogradely labeled CA1 neurons (red boxes) displayed at higher magnification.

(B) Examples of SB elicited in the Cg and PL by single electrical stimulation of the intermediate Hipp. Red arrows mark the electrical stimulus and the gray diamonds the evoked direct responses.

(C) Properties of SB evoked in the Cg and PL after single stimulation of the intermediate Hipp. Bar diagrams (mean ± SEM) depict the similar relative occurrence (left) and onset (right) in both prefrontal areas.

See also Figures S6–S8.

stimulation at 10 or 100 Hz was used. The effect of electrical stimulation on the CA1 region might be strengthened by costimulation of the neighboring alvear pathway (Deller et al., 1996). Remarkably, the occurrence of evoked SB increased on the anterior-posterior axis (Figure S7B), confirming that the density of functional projections to the PFC increases from the dorsal to ventral Hipp (Hoover and Vertes, 2007). These data indicate that hippocampal projections that innervate the neonatal PFC are an ideal candidate for mediating the hippocampal drive to the PFC.

Hippocampal Impairment Decreases Network Activity in the Neonatal PFC

To confirm the contribution of hippocampal drive to the generation of oscillatory rhythms in the neonatal PFC, three experimental approaches were additionally used. In the first instance, the intermediate and ventral but not dorsal Hipp were excitotoxically lesioned at P1, and the consequences on prefrontal-hippocampal networks were investigated at the end of the first postnatal week. Neonatal rats (n = 12) received a small volume (20–50 nl) of 40 mM NMDA (lesioned pups) or of 0.1 M PBS (sham pups) according to a previously described protocol (Lipska et al., 1993). The features of the NMDA-induced lesion were assessed post-mortem after Nissl staining. Characteristic cavitation, tissue loss, and gliosis (Bertrand et al., 2010) were present in lesioned pups, but not in the PBS-treated pups. The lesion extent, however, differed considerably across animals (Figures 8A and 8B). The CA1 and CA3 areas of the intermediate and ventral, but not dorsal Hipp were mainly affected. In some cases (n = 2), damage extended to the neighboring EC (Figure 8A). Moreover, lesions were mostly associated with a robust enlargement of the lateral ventricles.

Because an excitotoxic lesion may generally impair the development of pups by affecting their behavior and feeding abilities, we investigated the developmental milestones of PBS- and NMDA-treated animals. Their daily weight gain and general behavior (sleep-awake cycle, righting and grasping reflexes, feeding and locomotor behavior) were similar, indicating that the excitotoxic lesion did not impair the neonatal development. Whereas PBS treatment of the Hipp did not modify the features of prefrontal SB and NG, NMDA-induced lesion affected them. The occurrence of cingulate and prelimbic SB as well as of cingulate NG slightly decreased after hippocampal lesion, yet not at significant level. More prominent were the NMDA effects on the occurrence of prelimbic NG that decreased from 0.65 ± 0.16 bursts/min in PBS-treated pups to 0.06 ± 0.04 bursts/min ($p < 0.05$) (Figure 8C). The amplitude, duration, and main frequency of SB and NG did not change after NMDA lesion. Since NMDA treatment, even if identically performed, impaired to a different grade the Hipp of investigated pups (see Figure 8B), we assessed the relationship between the volume of NMDA-induced cavity and the occurrence of oscillatory events in the Cg and PL (n = 5 pups) (Figure 8D). Surprisingly, the occurrence of prefrontal activity did not linearly decrease with the size of hippocampal lesion, but as soon as the NMDA-induced cavity reached a certain volume (~0.5 mm^3) over the Hipp, the occurrence of SB and NG stabilized at a decreased level.

The main caveat of excitotoxic lesions, especially when performed in small-size neonatal animals, is their relative poor selectivity. To decide whether the diminishment of prelimbic NG is due, at least in part, to side-effect lesion of the EC or other neighboring areas, we used a second approach to impair the

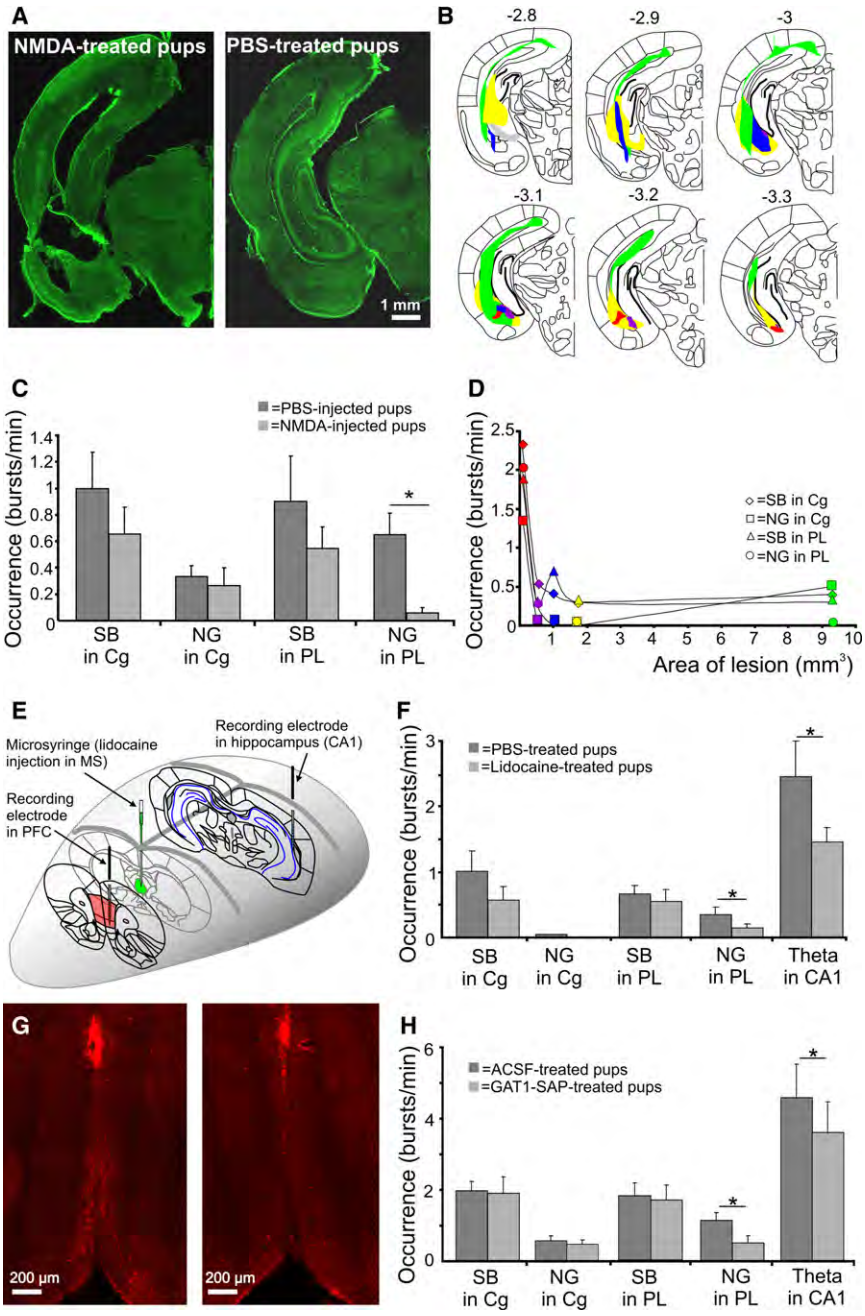

Figure 8. Consequences of Impaired Hippocampal Drive on the Early Prefrontal Patterns of Oscillatory Activity

(A) Photographs of representative Nissl-stained coronal sections across the intermediate Hipp of a P7 lesioned (NMDA-treated, left) and of a P7 sham (PBS-treated, right) rat. The section with the highest tissue loss after NMDA lesion is displayed. Note the typical hippocampal lesion characterized by neuronal loss, gliosis and enlarged ventricles.

(B) Diagrams reconstructing the position and size of the NMDA-induced lesion in successive coronal sections including the intermediate and ventral Hipp of 5 pups. The numbers refer to the age-corrected distance (mm) from Bregma. For each pup, the surface of lesion was marked with a different color.

(C) Bar diagram displaying the effects of hippocampal NMDA-induced lesion on the occurrence of oscillatory bursts recorded in the neonatal Cg and PL.

(D) Relationship between the size of NMDA-induced lesion and the occurrence of SB and NG in the Cg and PL of 5 P7–8 rats. The colors correspond to the diagrams shown in (B).

(E) Schematic drawing of the experimental paradigm allowing simultaneous recording of the PFC and intermediate Hipp before and after lidocaine-induced blockade of MS activity.

(F) Bar diagram displaying the effects of septal lidocaine treatment on the cingulate and prelimbic patterns of oscillatory activity as well as on the hippocampal theta oscillations recorded from 8 P6–8 pups.

(G) Photographs of representative coronal sections including the MS from P7 ACSF- (left) and GAT1-SAP-treated (right) pups that were stained for parvalbumin (red).

(H) Bar diagram displaying the effects of GAT1-SAP-induced impairment of septal GABAergic neurons on the cingulate and prelimbic patterns of oscillatory activity as well as on the hippocampal theta oscillations recorded from 8 P6–8 pups.

In (C), (F), and (H), data were displayed as mean ± SEM.

hippocampal drive. Discharge of the medial septum (MS) that has been reported to be one of the generators of CA1 theta rhythms in adult (Mizumori et al., 1989) was reversibly blocked by microinjections of lidocaine. Low volume (10–20 nl) of lidocaine was slowly applied in 4 P6–8 rats (Figure 8E). As consequence the occurrence of neonatal hippocampal theta bursts significantly ($p < 0.05$) and reversibly decreased from 2.5 ± 0.5 to 1.5 ± 0.2 bursts/min, indicating that the MS represents one generator also of neonatal theta bursts. Neither SPWs nor fast hippocampal rhythms were affected by lidocaine. The prefrontal patterns of activity were recorded simultaneously with the hippocampal activity before and after lidocaine treatment. Whereas SB were not influenced by lidocaine-induced diminishment of hippocampal theta activity, the occurrence of prelimbic NG decreased ($p < 0.05$) from 0.36 ± 0.11 to 0.16 ± 0.09 bursts/min (Figure 8F). The amplitude, duration and main frequency of prefrontal oscillations did not change after lidocaine injection.

Despite small injected volume and controlled application, lidocaine may spread from the injection site and nonselectively affect neighboring areas. To selectively impair the septal drive to the Hipp, we used a third experimental approach. As previously shown, septal GABAergic neurons contribute to the generation of adult hippocampal theta rhythm (Yoder and Pang, 2005). To identify their role for the immature theta bursts we selectively lesioned the septal GABAergic neurons by using the GABAergic

neurotoxin GABA-transporter-saporin (GAT1-SAP) that combines a rabbit polyclonal antibody to the GABA-transporter-1 with the ribosomal toxin saporin. Newborn rats (n = 8) received intraseptally a small volume (20–40 nl) of GAT-1 (325 ng/μl, 20 nl/min) or of vehicle (artificial cerebrospinal fluid, ACSF) according to a previously described protocol (Pang et al., 2010). Seven days later, the density of septal parvalbumin (PV)-positive neurons decreased from 123 ± 52.4 cells/mm^2 in ACSF-treated pups to 54.8 ± 8.6 cells/mm^2 in GAT1-SAP-treated pups (Figure 8G). The lesion of the septal GABAergic neurons reduced the occurrence of hippocampal theta bursts from 4.6 ± 0.9 to 3.6 ± 0.8 (n = 8 pups, $p < 0.05$). Consequently, the occurrence of prelimbic NG decreased from 1.1 ± 0.2 bursts/min in ACSF-treated pups to 0.6 ± 0.24 bursts/min ($p < 0.05$), while cingulate activity and prelimbic SB remained unaffected (Figure 8H).

The results of the three experimental approaches indicate that impairment of the Hipp, independently of the induction method, strongly reduces the early network activity of the PL.

DISCUSSION

Oscillatory entrainment of adult prefrontal-hippocampal networks seems to efficiently ensure reciprocal information transfer associated with mnemonic and executive functions. In the present study, we used multielectrode recordings to elucidate when and how this oscillatory entrainment between the PFC and Hipp develops through life and to get first insights into its mechanisms and function. We demonstrate here for the first time that the rat PFC starts to generate bursts of oscillatory activity with subregion-specific spatial and temporal organization during the first postnatal week. We additionally provide experimental evidence that this discontinuous prefrontal activity is driven via synaptic projections by hippocampal theta bursts. With ongoing maturation of the PFC and switch from discontinuous bursts to continuous theta-gamma rhythms, reciprocal interactions start to synchronize the prejuvenile prefrontal and hippocampal networks in theta oscillatory rhythms. These data indicate that the prefrontal and hippocampal networks maturate tightly correlated by transient coupling in oscillatory rhythms.

Developmental Profile of Network Activity in the PFC and Hipp

During the first two postnatal weeks, the network activity of the rodent PFC undergoes prominent changes, the initially generated discontinuous oscillations being replaced by continuous rhythms. This developmental time window corresponds to a period of massive cytoarchitectonic and functional reorganization of the PFC and its connectivity. Extending over approximately 3 weeks in rodents and until adolescence in humans (Flechsig, 1901; Van Eden and Uylings, 1985), the maturation of the PFC is significantly prolonged when compared with that of the primary sensory cortices. Correspondingly, the emergence of oscillatory bursts in the PFC, first observed at P3, is delayed when compared with the onset around birth of activity patterns in the V1 or S1 (Hanganu et al., 2006; Yang et al., 2009). These oscillations recorded in urethane-anesthetized rats mirror the physiological activity patterns of the developing PFC, since urethane anesthesia mimics the full spectrum of the natural sleep (Clement et al., 2008) and neonatal rats spend most of their time sleeping (Bolles and Woods, 1964). Therefore, it is not surprising that the incidence and most of the properties of neonatal SB were independent of the presence or level of urethane-anesthesia (see also Yang et al., 2009). Moreover, the properties of SB are similar to those of the spontaneous activity transients that have been electroencephalographically recorded in preterm human neonates of 29–31 weeks of postconceptional age (Vecchierini et al., 2007; Vanhatalo and Kaila, 2006).

The majority of neonatal SB seems to be generated in the upper part of the Cg as shown by the CSD analysis. The variability of their properties over the prefrontal subdivisions Cg and PL relates most likely to cytoarchitectonic features (e.g., homogenous versus heterogeneous structure of layer V in the Cg versus PL) (Van Eden and Uylings, 1985), different modulatory inputs or to distinct firing patterns of the two prefrontal areas. Toward the end of the first postnatal week, phase-locked gamma episodes superimpose the 4–12 Hz bursts. These prefrontal NG are also marginally affected by urethane anesthesia. They have not been reported in the neonatal primary sensory cortices. The superimposed short gamma episodes most likely mirror the activation of local prelimbic networks. However, the contribution of glutamatergic and GABAergic neurons in these networks remains largely unknown, since the differences in peak latencies and peak amplitude asymmetry, if any, between their spikes have not been investigated during development and only data for adult principal cells and interneurons are available (Barthó et al., 2004). Remarkably, these gamma episodes are clocked by the phase of the NG indicating that complex timing interactions control the firing of prefrontal neurons already during neonatal development.

Few days before the generation of SB and NG in the PFC, the intermediate Hipp shows also patterns of oscillatory activity. Our experimental data demonstrated the role of GABAergic input from the MS for the generation of neonatal theta bursts. Additionally, gap junctional coupling (Traub and Bibbig, 2000), nonhyperpolarizing $GABA_A$ receptor-mediated shunting-type inhibition and GABAergic hub neurons (Palva et al., 2000; Bonifazi et al., 2009) as well as upregulation of AMPA receptors toward the end of the first postnatal week may contribute to the generation of gamma oscillations and ripples in the neonatal Hipp.

With ongoing maturation, the activity of both PFC and Hipp switches from discontinuous bursts to continuous theta-gamma oscillations, the phase coupling of which seems to be less precise than in adult (Lisman and Buzsáki, 2008). This switch occurs almost simultaneously (~P10) in the prefrontal and primary sensory cortices (Colonnese and Khazipov, 2010) but delayed when compared with the Hipp. The continuous theta-gamma oscillations in the prejuvenile PFC differ in their synchronization patterns from the discontinuous network bursts in the neonatal PFC, indicating that distinct mechanisms underlie them. The switch from discontinuous to continuous activity in the PFC coincides with the formation of layer II and III, the progressive disappearance of the CP, and the initiation of prejuvenile synaptic pruning refining the exuberant intra- and

intercortical as well as corticosubcortical projections (Van Eden and Uylings, 1985).

Entrainment of Prefrontal-Hippocampal Networks during Postnatal Development

One of the major findings of the present study is that the Hipp drives the intermittent oscillatory activity in the neonatal PFC. Our simultaneous recordings from the PFC and Hipp as well as stimulation and lesion experiments provide consistent pieces of evidence for the theta entrainment of developing prefrontal-hippocampal networks at every investigated level: (1) network interactions, (2) coupling of individual neurons to theta network rhythm, and (3) timed coactivation of single prefrontal and hippocampal neurons.

At network level, high theta-frequency coherence of oscillations in the neonatal PFC and Hipp argues for a tight and stable coactivation of the two areas. The caveats inherent to experiments relying on FP recordings seem to not query this conclusion. First, unspecific volume synchrony was disproved by the coherence between prefrontal MUA and hippocampal FP and by the significantly different dominant frequencies of hippocampal theta bursts and prefrontal oscillations. Second, the significantly lower level of coupling between the primary sensory cortices and Hipp than between the PFC and Hipp argues against general entrainment of all cortical areas in oscillatory rhythms.

As consequence of their early coactivation, manipulation of hippocampal networks by different means affected the prefrontal activity. Hippocampal activation by electrical stimulation of the CA1 area elicited prefrontal bursts with latencies of 80–100 ms, suggesting that the prefrontal-hippocampal coactivation relies on synaptic connectivity. Hippocampal impairment induced either by excitotoxic NMDA injection into the CA1 area or by septal damage decreased the network activity of the neonatal PFC, especially of the PL. In the light of similar consequences of different lesion methods on the PL it is very likely that the contribution of method-specific side-effects (e.g., morphological and/or functional impairment outside the CA1 area) is very limited. Minimization of side effects has been achieved by optimally choosing the coordinates, volume and speed of injection.

The neonatal prefrontal-hippocampal networks are not only coactivated during oscillatory activity, but their interactions show clear directionality. According to the Granger causality analysis, the increased theta-band coherence during bursts is a consequence of the higher information flow between the two areas, with a generally stronger drive from the Hipp to PL during neonatal development. The capability of prelimbic neurons to fire with phase preference to hippocampal theta rhythm supports these causal interactions. Additionally, it represents a possible mechanism, how these two distant areas work together during development. In contrast to the extensive prefrontal-hippocampal coupling in adult (Siapas et al., 2005; Hyman et al., 2005; Wierzynski et al., 2009), only ~9% of the neonatal neurons in the PFC are phase-locked to the hippocampal theta rhythm. Nevertheless, the mechanisms of phase-locking are similar during early development and at adulthood, theta entrainment of prelimbic neurons involving the excitatory projections from the CA1 area of the intermediate and ventral Hipp. The short latencies of electrically evoked responses in the neonatal PL were consistent with the conduction time of hippocampal-prefrontal pathway (Tierney et al., 2004). However, neither the stimulation experiments nor the Granger analysis can reliably decide whether only such monosynaptic pathways drive the information from the Hipp to PFC or whether third areas, like the EC or thalamus (Steriade and McCarley, 1990; Vertes, 2006), are equally involved.

Analysis of the spike-timing relationship between individual cell pairs in the two areas provided better understanding of the early communication between the PFC and Hipp. Multitetrode recordings in neonatal rodents revealed that the prefrontal firing may be driven at delays corresponding to monosynaptic projections by the hippocampal discharge. Such interpretation must, however, be tempered by the caveats of the cross-covariance analysis when applied to neonatal data. The low firing rate of prefrontal neurons not only dramatically reduced the number of cell pairs suitable for the analysis, but also facilitated the detection of spurious cross-covariances (Siapas et al., 2005).

The spike-timing interactions in prejuvenile prefrontal-hippocampal networks are supportive for the conclusions of the Granger analysis. The presence of prefrontal neurons firing shortly before or after the hippocampal cells argues for mutually interacting PFC and Hipp. Whether the directional change between neonatal and prejuvenile development is related to the strong network refinement and pruning during adolescence remains to be elucidated.

Functional Relevance of Early Oscillatory Coupling within Prefrontal-Hippocampal Networks

Previous studies have shown that bursts of oscillatory activity are present in the neonatal primary sensory cortices (Khazipov et al., 2004; Hanganu et al., 2006; Yang et al., 2009), where they may act as a template facilitating the refinement of cortical maps (barrels, ocular dominance columns) (Dupont et al., 2006; Yang et al., 2009).

The intrinsic properties, spatial and temporal organization as well as most likely the underlying mechanisms and the function distinguish the prefrontal oscillatory bursts from those recorded in the S1 or V1 (Hanganu-Opatz, 2010). Differences were noted also between the prefrontal areas Cg and PL. We propose that one of the factors leading to these differences is the area-specific impact of hippocampal drive. Early generated hippocampal theta bursts drive the prelimbic network by timing the gamma phase-locked neuronal firing within local networks and modulate to a lesser extent the cingulate activity. This different impact of hippocampal drive on the Cg versus PL is present also at adulthood, the cingulate activity being able to emerge independently of the Hipp (Leung and Borst, 1987).

The question that arises is why such strong and directed coupling exists between the PL and Hipp at early stages of development. In the adult brain temporal entrainment of prelimbic-hippocampal networks that takes place during specific behavioral epochs has been described as the main mechanism underlying the transfer and storage of information, thus underlying the mnemonic and executive abilities of animals and humans (Siapas and Wilson, 1998; Sirota et al., 2008; Hyman

et al., 2010). For example, the coupling between the PL and Hipp as well as the portion of phase-locked prefrontal neurons increases during anxiety-like behavior and during working or spatial memory tasks (Adhikari et al., 2010; Hyman et al., 2010; Moran et al., 2010). Functional basis of this behaviorally relevant coupling are the direct monosynaptic projections timing the prefrontal and hippocampal firing (Siapas et al., 2005) as well as the PFC organization in hypercolumns that are globally "pushed" by the hippocampal input during the task (Hasselmo, 2005; Hyman et al., 2005). During development the strong prefrontal-hippocampal communication is not related to an overt behavioral task, but takes place during sleep. We propose that the oscillatory drive from the Hipp facilitates not only the morphological and functional development of the PFC but enables also the refinement of the behaviorally relevant communication scaffold between the two areas. Neonatal prelimbic neurons receive via synaptic projections theta-phase modulated inputs from the Hipp and start to tune their firing. As long as the functional hypercolumns amplifying the hippocampal signal in the PFC are not fully refined, a very low number of prefrontal neurons seems to be clocked by the Hipp and may act as a sort of "hub" that organizes the local networks (Bonifazi et al., 2009). This hippocampus-timed gamma entrainment of local networks may shape and plastically modify the prelimbic connectivity. The PFC reaches its functional maturation during adolescence by undergoing an intense reorganization and pruning of connectivity under the influence of various neurotransmitters. At this developmental stage the PFC and Hipp are still synchronized and theta entrained, but their network and cell-to-cell interactions are not unidirectional anymore. The temporary loss of precision within juvenile prefrontal-hippocampal communication may represent one of the mechanisms contributing to impulsive and uncontrolled behavior during adolescence (Casey et al., 2008).

Because the early theta drive from the Hipp seems to be mandatory for the refinement of functional organization within the PFC and for precise prefrontal-hippocampal interactions, this developmental period corresponding to the second and third trimester of gestation in humans (Clancy et al., 2001) may be considered as critical period for the maturation of mnemonic and executive abilities. Weaker or delayed theta-modulated drive from the Hipp to the PFC during this period may lead to lifelong miswiring and abnormal entrainment of prefrontal-hippocampal networks. Remarkably, such abnormal communication between the PFC and Hipp is the central pathophysiological feature of neuropsychiatric disorders (e.g., schizophrenia) that accounts for attention, working memory, and decision-making deficits (Loveland et al., 2008; Sigurdsson et al., 2010; Uhlhaas and Singer, 2010).

EXPERIMENTAL PROCEDURES

Surgical Preparation

All experiments were performed in compliance with the German laws and the guidelines of the European Community for the use of animals in research and were approved by the local ethical committee. Extracellular recordings were performed in the PFC and intermediate Hipp of P0–14 male rats and in the S1 and V1 of P0–3 male rats using experimental protocols as described previously (Hanganu et al., 2006; Yang et al., 2009).

Recording and Stimulation Protocols

Simultaneous recordings of FP and MUA were performed from the PFC and Hipp using one-shank and four-shank 8- or 16-channel Michigan electrodes as well as multitetrodes. For electrical stimulation of the Hipp, single or trains of electrical pulses were applied via a bipolar tungsten electrode inserted into the CA1 area of the Hipp. The recording and stimulation protocols are described in detail in Supplemental Information.

Impairment of Hippocampal Activity

Acute and reversible impairment of hippocampal activity was obtained by injection of lidocaine into the MS of P6–8 male rats. For chronic impairment of hippocampal drive to the PFC, either excitotoxic lesion of intermediate/ventral, but not dorsal Hipp, using NMDA or selective lesion of septal GABAergic neurons using GAT1-SAP was induced. For details, see Supplemental Information.

Data Analysis

Data were imported and analyzed off-line using custom-written tools in Matlab software version 7.7 (Mathworks, Natick, MA). For details, see Supplemental Information.

Statistics

Data in the text are presented as mean ± SEM and displayed as bar diagrams, histograms, and polar plots. Statistical analyses were performed with SPSS 15.0/Systat software (SPSS GmbH, Munich, Germany). All values were tested for normal distribution by the Kolmogorov-Smirnov test, except their low number ($n < 10$) precluded reliable testing. For normally distributed values paired or unpaired t test was used. For low number of values or not normally distributed values nonparametric tests (Mann-Whitney-Wilcoxon test) were used. For some data sets multiple ANOVA tests and regression analysis were performed. Significance levels of $p < 0.05$ (*), $p < 0.01$ (**), or $p < 0.001$ (***) were detected.

Retrograde Tracing and Staining Protocols

Male Wistar rats received at P1 or P6 bilateral injections of FG into the PFC. Parvalbumin (PV) immunoreactivity was revealed using rabbit anti-PV IgG (1:1000). For details, see Supplemental Information.

SUPPLEMENTAL INFORMATION

Supplemental Information includes eight figures, three tables, and Supplemental Experimental Procedures and can be found with this article online at doi:10.1016/j.neuron.2011.05.041.

ACKNOWLEDGMENTS

We thank Drs. M. Denker, T. Siapas, A. Sirota, and M. Ding for valuable discussions, Drs. A. Draguhn, S. Grün, and W. Kilb for helpful suggestions and comments on the manuscript, and Dr. G. Schneider and G. Meckenhäuser for assistance on statistics. I.L.H.-O. acknowledges support by the Emmy Noether-Program of German Research Foundation (Ha4466/3-1) and the German Federal Ministry of Education and Research (01GQ0809).

Accepted: May 5, 2011
Published: July 27, 2011

REFERENCES

Adhikari, A., Topiwala, M.A., and Gordon, J.A. (2010). Synchronized activity between the ventral hippocampus and the medial prefrontal cortex during anxiety. Neuron *65*, 257–269.

Anderson, K.L., Rajagovindan, R., Ghacibeh, G.A., Meador, K.J., and Ding, M. (2010). Theta oscillations mediate interaction between prefrontal cortex and medial temporal lobe in human memory. Cereb. Cortex *20*, 1604–1612.

Angevine, J.B. (1975). Development of the hippocampal formation. In The hippocampus, R.L. Isaacson and K.H. Pribram, eds. (New York: Plenum Press), pp. 61–90.

Barthó, P., Hirase, H., Monconduit, L., Zugaro, M., Harris, K.D., and Buzsáki, G. (2004). Characterization of neocortical principal cells and interneurons by network interactions and extracellular features. J. Neurophysiol. *92*, 600–608.

Bertrand, J.B., Langlois, J.B., Bégou, M., Volle, J., Brun, P., d'Amato, T., Saoud, M., and Suaud-Chagny, M.F. (2010). Longitudinal MRI monitoring of brain damage in the neonatal ventral hippocampal lesion rat model of schizophrenia. Hippocampus *20*, 264–278.

Bolles, R.C., and Woods, P.J. (1964). The ontogeny of the behaviour in the albino rat. Anim. Behav. *12*, 427–441.

Bonifazi, P., Goldin, M., Picardo, M.A., Jorquera, I., Cattani, A., Bianconi, G., Represa, A., Ben-Ari, Y., and Cossart, R. (2009). GABAergic hub neurons orchestrate synchrony in developing hippocampal networks. Science *326*, 1419–1424.

Buzsáki, G. (2006). Rhythms of the Brain (Oxford: Oxford University Press).

Buzsáki, G., and Draguhn, A. (2004). Neuronal oscillations in cortical networks. Science *304*, 1926–1929.

Buzsáki, G., Horváth, Z., Urioste, R., Hetke, J., and Wise, K. (1992). High-frequency network oscillation in the hippocampus. Science *256*, 1025–1027.

Casey, B.J., Jones, R.M., and Hare, T.A. (2008). The adolescent brain. Ann. N Y Acad. Sci. *1124*, 111–126.

Clancy, B., Darlington, R.B., and Finlay, B.L. (2001). Translating developmental time across mammalian species. Neuroscience *105*, 7–17.

Clement, E.A., Richard, A., Thwaites, M., Ailon, J., Peters, S., and Dickson, C.T. (2008). Cyclic and sleep-like spontaneous alternations of brain state under urethane anaesthesia. PLoS ONE *3*, e2004. 10.1371/journal.pone.0002004.

Colonnese, M.T., and Khazipov, R. (2010). "Slow activity transients" in infant rat visual cortex: a spreading synchronous oscillation patterned by retinal waves. J. Neurosci. *30*, 4325–4337.

Deller, T., Adelmann, G., Nitsch, R., and Frotscher, M. (1996). The alvear pathway of the rat hippocampus. Cell Tissue Res. *286*, 293–303.

Ding, M., Bressler, S.L., Yang, W., and Liang, H. (2000). Short-window spectral analysis of cortical event-related potentials by adaptive multivariate autoregressive modeling: data preprocessing, model validation, and variability assessment. Biol. Cybern. *83*, 35–45.

Dreyfus-Brisac, C. (1962). The electroencephalogram of the premature infant. World Neurol. *3*, 5–15.

Dupont, E., Hanganu, I.L., Kilb, W., Hirsch, S., and Luhmann, H.J. (2006). Rapid developmental switch in the mechanisms driving early cortical columnar networks. Nature *439*, 79–83.

Euston, D.R., Tatsuno, M., and McNaughton, B.L. (2007). Fast-forward playback of recent memory sequences in prefrontal cortex during sleep. Science *318*, 1147–1150.

Flechsig, P. (1901). Developmental (myelogenetic) localization of the cerebral cortex in human subject. Lancet *2*, 1027–1029.

Hanganu, I.L., Ben-Ari, Y., and Khazipov, R. (2006). Retinal waves trigger spindle bursts in the neonatal rat visual cortex. J. Neurosci. *26*, 6728–6736.

Hanganu-Opatz, I.L. (2010). Between molecules and experience: role of early patterns of coordinated activity for the development of cortical maps and sensory abilities. Brain Res. Brain Res. Rev. *64*, 160–176.

Hasselmo, M.E. (2005). What is the function of hippocampal theta rhythm?—Linking behavioral data to phasic properties of field potential and unit recording data. Hippocampus *15*, 936–949.

Hoover, W.B., and Vertes, R.P. (2007). Anatomical analysis of afferent projections to the medial prefrontal cortex in the rat. Brain Struct. Funct. *212*, 149–179.

Huberman, A.D., Speer, C.M., and Chapman, B. (2006). Spontaneous retinal activity mediates development of ocular dominance columns and binocular receptive fields in v1. Neuron *52*, 247–254.

Hyman, J.M., Zilli, E.A., Paley, A.M., and Hasselmo, M.E. (2005). Medial prefrontal cortex cells show dynamic modulation with the hippocampal theta rhythm dependent on behavior. Hippocampus *15*, 739–749.

Hyman, J.M., Zilli, E.A., Paley, A.M., and Hasselmo, M.E. (2010). Working memory performance correlates with prefrontal-hippocampal theta interactions but not with prefrontal neuron firing rates. Front. Integr. Neurosci. *4*, 2.

Khazipov, R., Sirota, A., Leinekugel, X., Holmes, G.L., Ben-Ari, Y., and Buzsáki, G. (2004). Early motor activity drives spindle bursts in the developing somatosensory cortex. Nature *432*, 758–761.

Lachaux, J.P., Rodriguez, E., Martinerie, J., and Varela, F.J. (1999). Measuring phase synchrony in brain signals. Hum. Brain Mapp. *8*, 194–208.

Lahtinen, H., Palva, J.M., Sumanen, S., Voipio, J., Kaila, K., and Taira, T. (2002). Postnatal development of rat hippocampal gamma rhythm in vivo. J. Neurophysiol. *88*, 1469–1474.

Le Van Quyen, M., Bragin, A., Staba, R., Crépon, B., Wilson, C.L., and Engel, J., Jr. (2008). Cell type-specific firing during ripple oscillations in the hippocampal formation of humans. J. Neurosci. *28*, 6104–6110.

Leung, L.W., and Borst, J.G. (1987). Electrical activity of the cingulate cortex. I. Generating mechanisms and relations to behavior. Brain Res. *407*, 68–80.

Lipska, B.K., Jaskiw, G.E., and Weinberger, D.R. (1993). Postpubertal emergence of hyperresponsiveness to stress and to amphetamine after neonatal excitotoxic hippocampal damage: a potential animal model of schizophrenia. Neuropsychopharmacology *9*, 67–75.

Lisman, J., and Buzsáki, G. (2008). A neural coding scheme formed by the combined function of gamma and theta oscillations. Schizophr. Bull. *34*, 974–980.

Loveland, K.A., Bachevalier, J., Pearson, D.A., and Lane, D.M. (2008). Fronto-limbic functioning in children and adolescents with and without autism. Neuropsychologia *46*, 49–62.

Miller, E.K. (2000). The prefrontal cortex and cognitive control. Nat. Rev. Neurosci. *1*, 59–65.

Mizumori, S.J., Barnes, C.A., and McNaughton, B.L. (1989). Reversible inactivation of the medial septum: selective effects on the spontaneous unit activity of different hippocampal cell types. Brain Res. *500*, 99–106.

Mohns, E.J., and Blumberg, M.S. (2008). Synchronous bursts of neuronal activity in the developing hippocampus: modulation by active sleep and association with emerging gamma and theta rhythms. J. Neurosci. *28*, 10134–10144.

Mohns, E.J., and Blumberg, M.S. (2010). Neocortical activation of the hippocampus during sleep in infant rats. J. Neurosci. *30*, 3438–3449.

Moran, R.J., Campo, P., Maestu, F., Reilly, R.B., Dolan, R.J., and Strange, B.A. (2010). Peak frequency in the theta and alpha bands correlates with human working memory capacity. Front. Hum. Neurosci. *4*, 200.

Palva, J.M., Lamsa, K., Lauri, S.E., Rauvala, H., Kaila, K., and Taira, T. (2000). Fast network oscillations in the newborn rat hippocampus *in vitro*. J. Neurosci. *20*, 1170–1178.

Pang, K.C., Jiao, X., Sinha, S., Beck, K.D., and Servatius, R.J. (2010). Damage of GABAergic neurons in the medial septum impairs spatial working memory and extinction of active avoidance: effects on proactive interference. Hippocampus *2010*, 17.

Siapas, A.G., and Wilson, M.A. (1998). Coordinated interactions between hippocampal ripples and cortical spindles during slow-wave sleep. Neuron *21*, 1123–1128.

Siapas, A.G., Lubenov, E.V., and Wilson, M.A. (2005). Prefrontal phase locking to hippocampal theta oscillations. Neuron *46*, 141–151.

Sigurdsson, T., Stark, K.L., Karayiorgou, M., Gogos, J.A., and Gordon, J.A. (2010). Impaired hippocampal-prefrontal synchrony in a genetic mouse model of schizophrenia. Nature *464*, 763–767.

Sirota, A., Montgomery, S., Fujisawa, S., Isomura, Y., Zugaro, M., and Buzsáki, G. (2008). Entrainment of neocortical neurons and gamma oscillations by the hippocampal theta rhythm. Neuron *60*, 683–697.

Soteropoulos, D.S., and Baker, S.N. (2006). Corticocerebellar coherence during a precision grip task in the monkey. J. Neurophysiol. *95*, 1194–1206.

Steriade, M., and McCarley, R.W. (1990). Brainstem Control of Wakefulness and Sleep (New York: Plenum Press).

Swanson, L.W. (1981). A direct projection from Ammon's horn to prefrontal cortex in the rat. Brain Res. *217*, 150–154.

Thierry, A.M., Gioanni, Y., Dégénétais, E., and Glowinski, J. (2000). Hippocampo-prefrontal cortex pathway: anatomical and electrophysiological characteristics. Hippocampus *10*, 411–419.

Tierney, P.L., Dégenètais, E., Thierry, A.M., Glowinski, J., and Gioanni, Y. (2004). Influence of the hippocampus on interneurons of the rat prefrontal cortex. Eur. J. Neurosci. *20*, 514–524.

Traub, R.D., and Bibbig, A. (2000). A model of high-frequency ripples in the hippocampus based on synaptic coupling plus axon-axon gap junctions between pyramidal neurons. J. Neurosci. *20*, 2086–2093.

Uhlhaas, P.J., and Singer, W. (2010). Abnormal neural oscillations and synchrony in schizophrenia. Nat. Rev. Neurosci. *11*, 100–113.

Vanhatalo, S., and Kaila, K. (2006). Development of neonatal EEG activity: from phenomenology to physiology. Semin. Fetal Neonatl. Med *11*, 471–478.

Van Eden, C.G., and Uylings, H.B. (1985). Cytoarchitectonic development of the prefrontal cortex in the rat. J. Comp. Neurol. *241*, 253–267.

Vecchierini, M.F., André, M., and d'Allest, A.M. (2007). Normal EEG of premature infants born between 24 and 30 weeks gestational age: terminology, definitions and maturation aspects. Neurophysiol. Clin. *37*, 311–323.

Vertes, R.P. (2006). Interactions among the medial prefrontal cortex, hippocampus and midline thalamus in emotional and cognitive processing in the rat. Neuroscience *142*, 1–20.

Wierzynski, C.M., Lubenov, E.V., Gu, M., and Siapas, A.G. (2009). State-dependent spike-timing relationships between hippocampal and prefrontal circuits during sleep. Neuron *61*, 587–596.

Womelsdorf, T., Schoffelen, J.M., Oostenveld, R., Singer, W., Desimone, R., Engel, A.K., and Fries, P. (2007). Modulation of neuronal interactions through neuronal synchronization. Science *316*, 1609–1612.

Yang, J.W., Hanganu-Opatz, I.L., Sun, J.J., and Luhmann, H.J. (2009). Three patterns of oscillatory activity differentially synchronize developing neocortical networks in vivo. J. Neurosci. *29*, 9011–9025.

Yoder, R.M., and Pang, K.C. (2005). Involvement of GABAergic and cholinergic medial septal neurons in hippocampal theta rhythm. Hippocampus *15*, 381–392.

Neuron, Volume 71

Supplemental Information

Coupled Oscillations Mediate Directed Interactions between Prefrontal Cortex and Hippocampus of the Neonatal Rat

Marco D. Brockmann, Beatrice Pöschel, Nicole Cichon, and Ileana L. Hanganu-Opatz

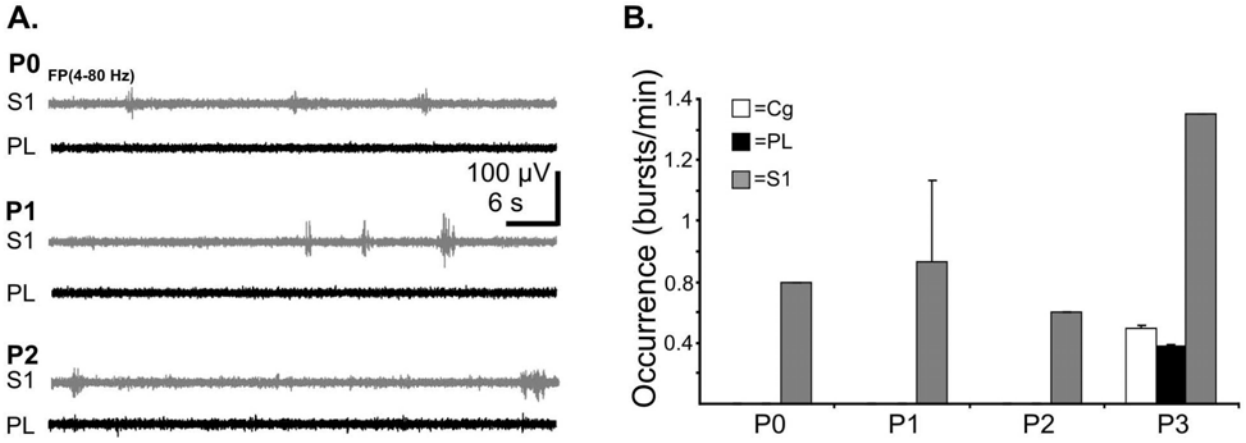

Figure S1. Emergence of oscillatory activity in the PFC and S1. (A) Simultaneous extracellular FP recordings from the PFC (black) and S1 (gray) of a P0 (top), P1 (middle) and P2 (bottom) rat. Note the progressive increase in the amplitude and duration of oscillatory bursts in the S1 and the absence of network activity in the PFC. (B) Delayed emergence of oscillatory activity in the neonatal PFC compared with the S1. Bar diagram (mean ± SEM) displaying the occurrence of SB in the Cg (white), PL (black) and S1 (grey) of 11 rats during the first four postnatal days.

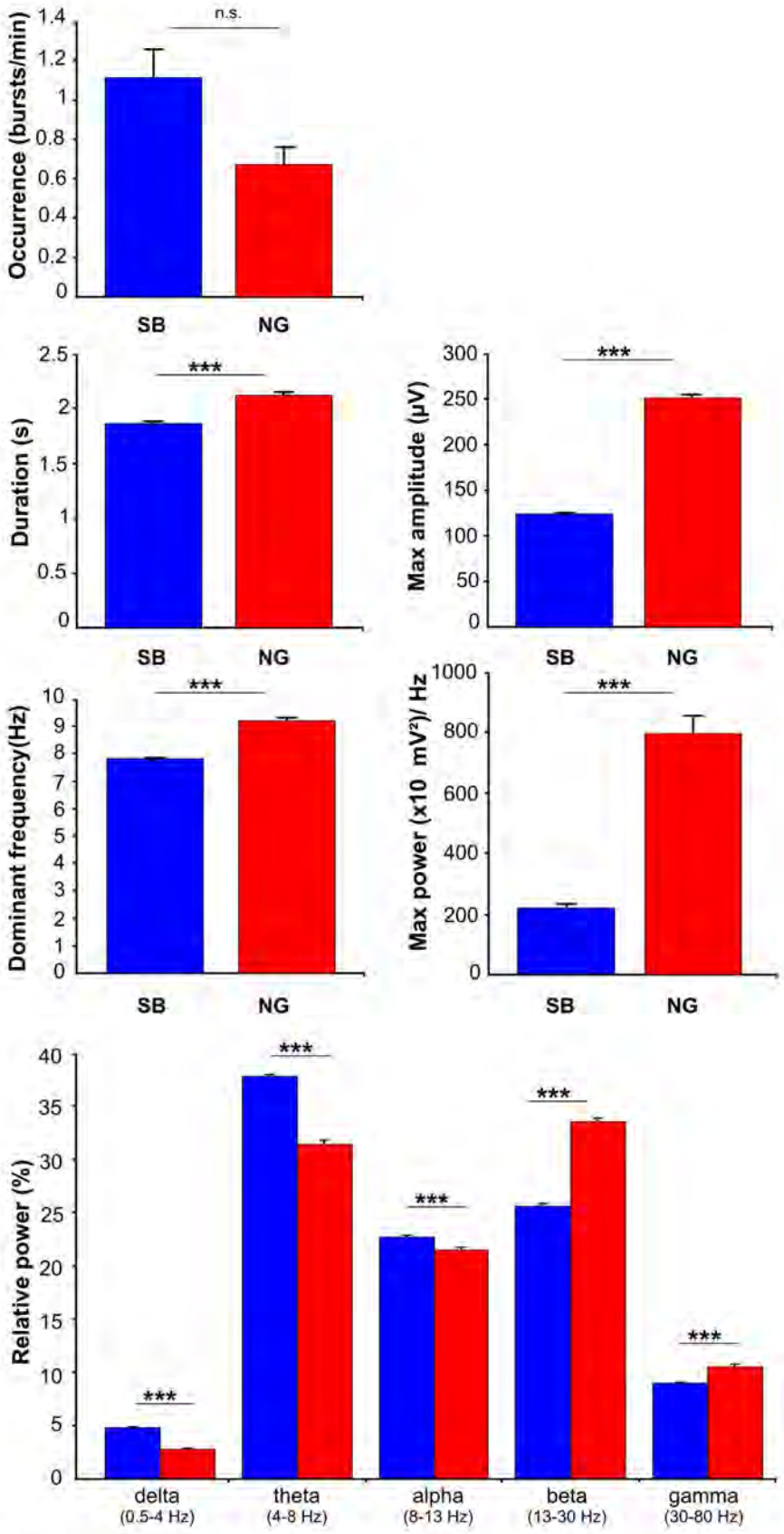

Figure S2. Properties of SB and NG in the neonatal PFC of the rat. Bar diagrams displaying the occurrence, duration, maximal amplitude, dominant frequency, and maximal power as well as the relative power in different frequency bands for SB (blue) and NG (red). Data from 27 pups were averaged over the entire PFC and displayed as mean ± SEM.

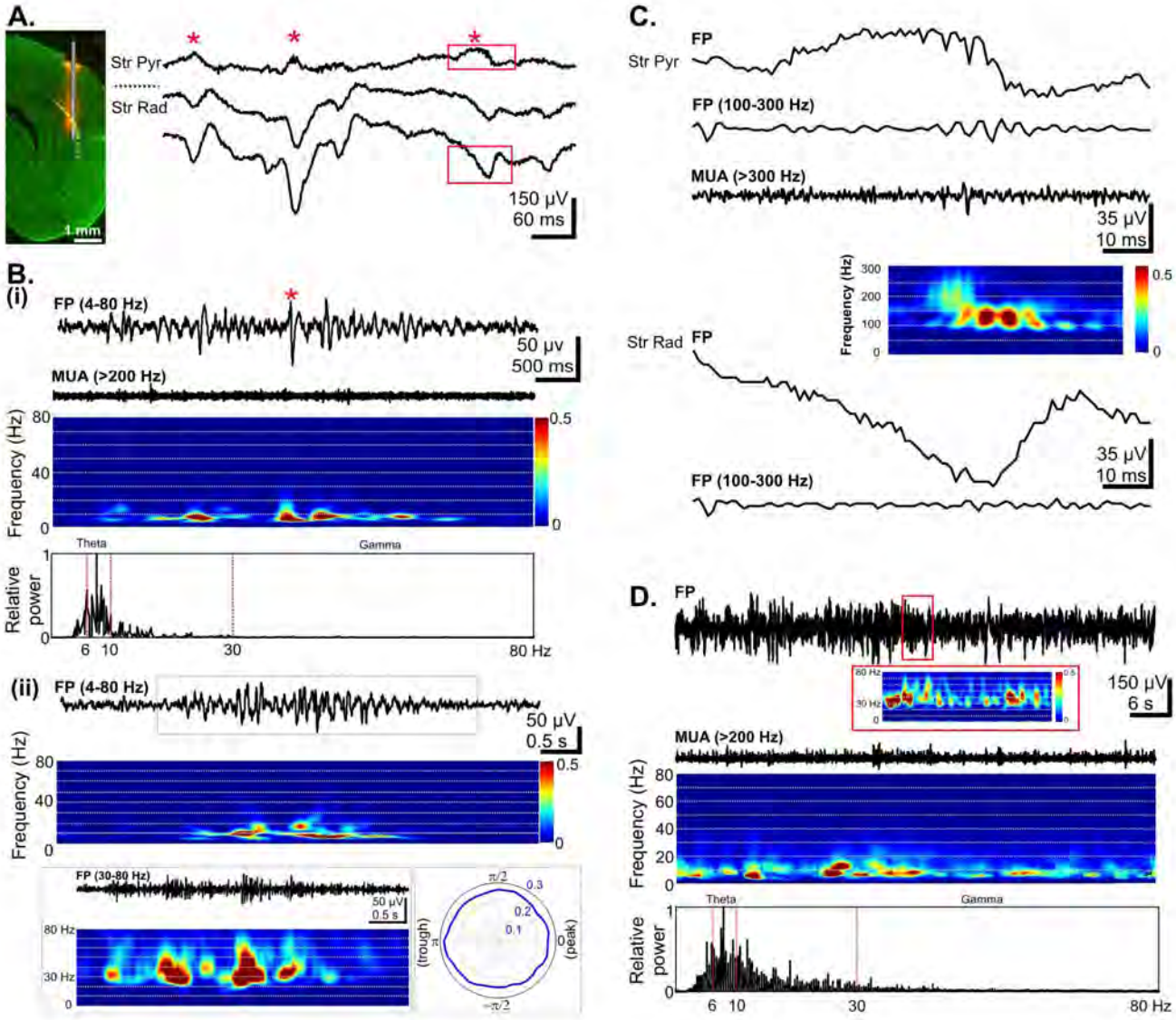

Figure S3. Patterns of oscillatory activity in the CA1 area of the intermediate Hipp *in vivo* during the first two postnatal weeks. (A) Left, digital photomontage reconstructing the location of the DiI-labeled recording electrode (orange) in the CA1 region of a Nissl-stained 100 µm-thick coronal section (green) from a P8 rat. The superimposed yellow dots summarize the location of recordings sites on similar anterior-posterior coordinates in 34 out of 83 investigated pups. Right, extracellular FP recording of prominent SPWs (marked by red asterisks) reversing between Str Pyr and Str Rad. (B) (i) Characteristic CA1 theta burst with superimposed SPW (red asterisk) displayed after band-pass (4-80 Hz) filtering (top) and the corresponding MUA after 200 Hz high-pass filtering. Color-coded frequency plot shows the wavelet spectrum of the FP at identical time scale. Fast Fourier transformation of the FP illustrates the relative power of the theta bursts with maximal frequency ~ 8 Hz (bottom). (ii) Characteristic CA1 theta burst with superimposed gamma episodes displayed after band-pass (30-80 Hz) filtering at larger temporal resolution (inset left). Color-coded frequency plot shows the wavelet spectrum of the FP at identical time scale. Inset right, polar plot displaying the uniform distribution of gamma episodes on the theta cycle. (C) Characteristic ripples in Str Pyr superimposed on the SPW [top, red box in (A)] accompanied by corresponding MUA after 300 Hz high-pass filtering and the color-coded wavelet plot at identical time scale. Simultaneously recorded SPW in Str rad displayed before and after band-pass (100-300 Hz) filtering (bottom) reveals the absence of superimposed ripples. (D) Extracellular FP recording of the continuous oscillatory activity from the CA1 area of a P14 rat (top) and the corresponding MUA after 200 Hz high-pass filtering (below). The wavelet spectrum (bottom) reveals the prominent activity below 10 Hz. Inset, wavelet spectrum for a segment of the recording demonstrating the presence of periodic superimposed gamma episodes with main frequency ~ 30 Hz.

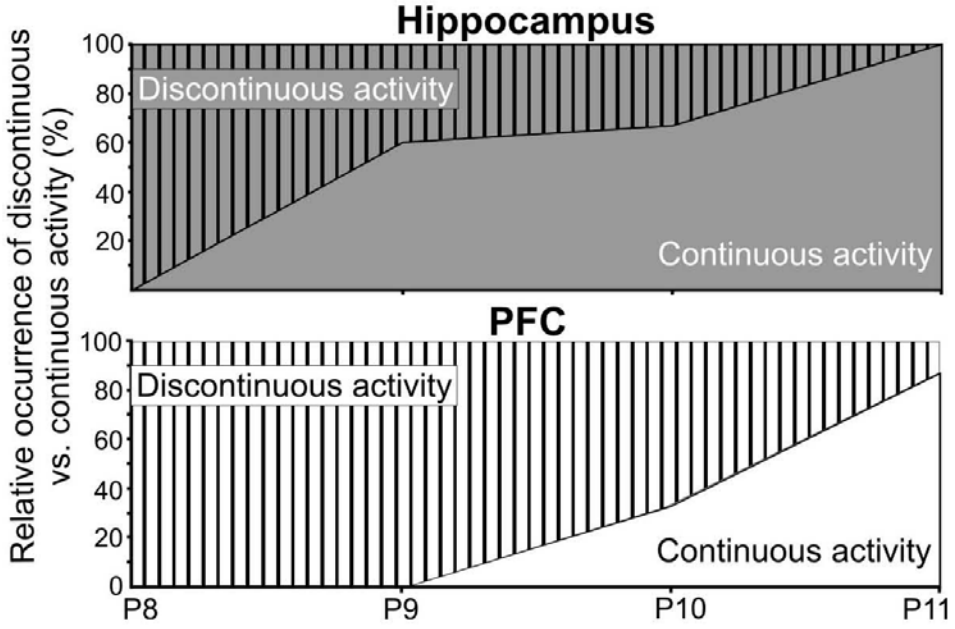

Figure S4. Transition from discontinuous to continuous activity in the developing PFC and Hipp. Diagram displaying the relative number of pups showing discontinuous vs. continuous oscillations in the PFC and Hipp. The number of pups with continuous or discontinuous activity in the PFC and Hipp was normalized to the total number of pups and displayed for the developmental period P8-11. Note the earlier switch to continuous activity in the Hipp than in the PFC.

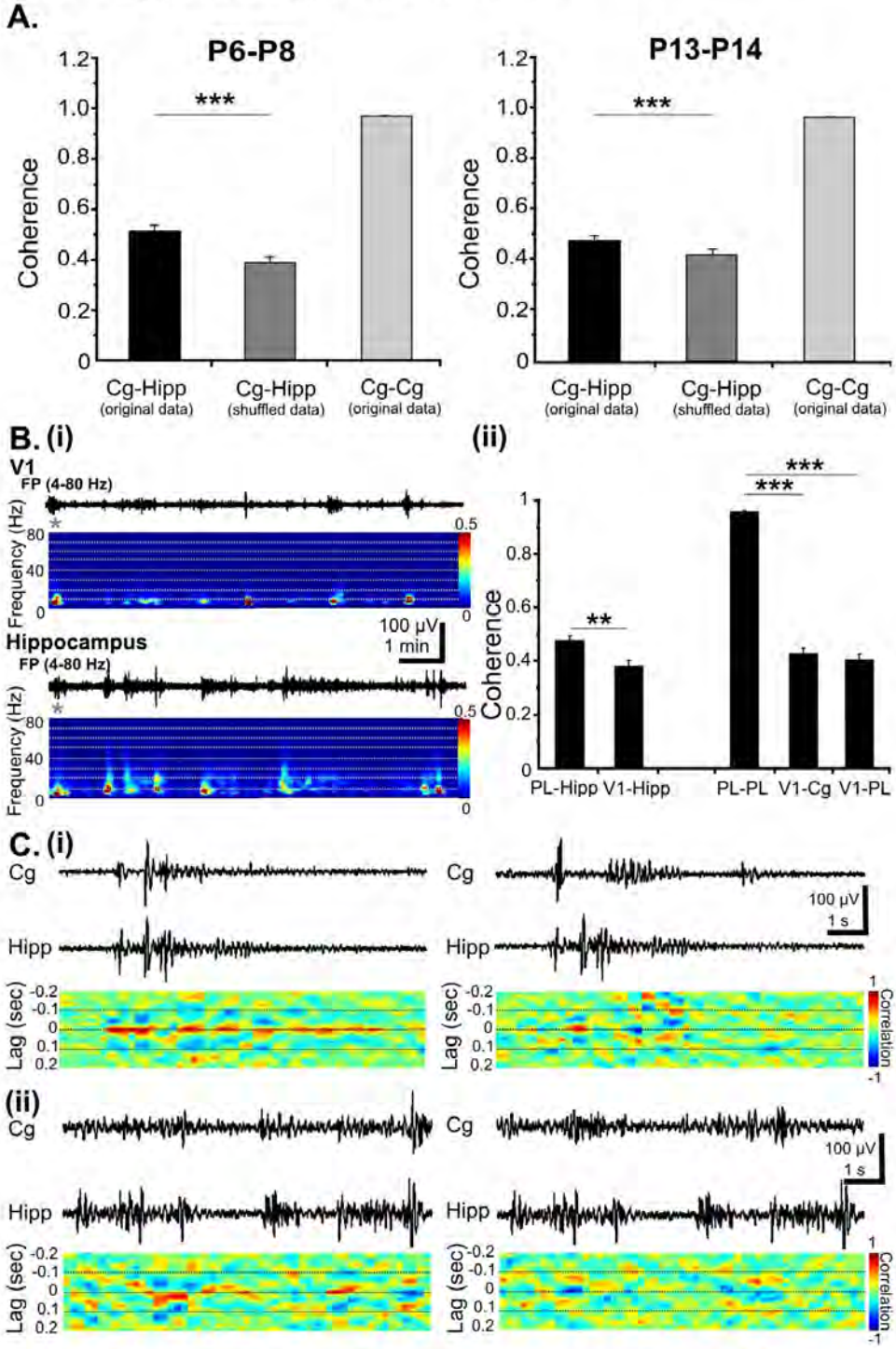

Figure S5. Dynamic coupling of oscillatory activity in the Hipp, prefrontal and primary visual cortices during development. (A) Coherence of Cg-CA1 oscillations calculated for intermittent (left) and continuous (right) activity from 6 P6-8 pups and 6 P13-14 pups, respectively. Bar diagrams (mean ± SEM) reveal the significantly higher Cg-hippocampal coherence for original than for shuffled data. Note the relatively invariable and very high coherence within the Cg at both investigated developmental stages. (B) (i) Simultaneous FP recordings of the discontinuous oscillatory activity in the V1 and CA1 area of the intermediate Hipp accompanied by the color-coded wavelet spectra of the FP at identical time scale. Note the low incidence of simultaneously occurring (gray asterisks) hippocampal theta oscillations and visual SB. (ii) Coherence of oscillatory events between different cortical areas. (C) Dynamics of Cg-hippocampal coupling. (i) Simultaneous FP recordings of oscillatory activity in the Cg and hippocampal CA1 of a P7 rat and the time-aligned sliding cross-correlograms for original (left) and shuffled (right) data. (ii) Same as (i) for continuous activity from a P13 rat where the peak correlation at time lag 0 ms vaxes and vanes. All other colors than green represent positive (red) or negative (blue) correlation.

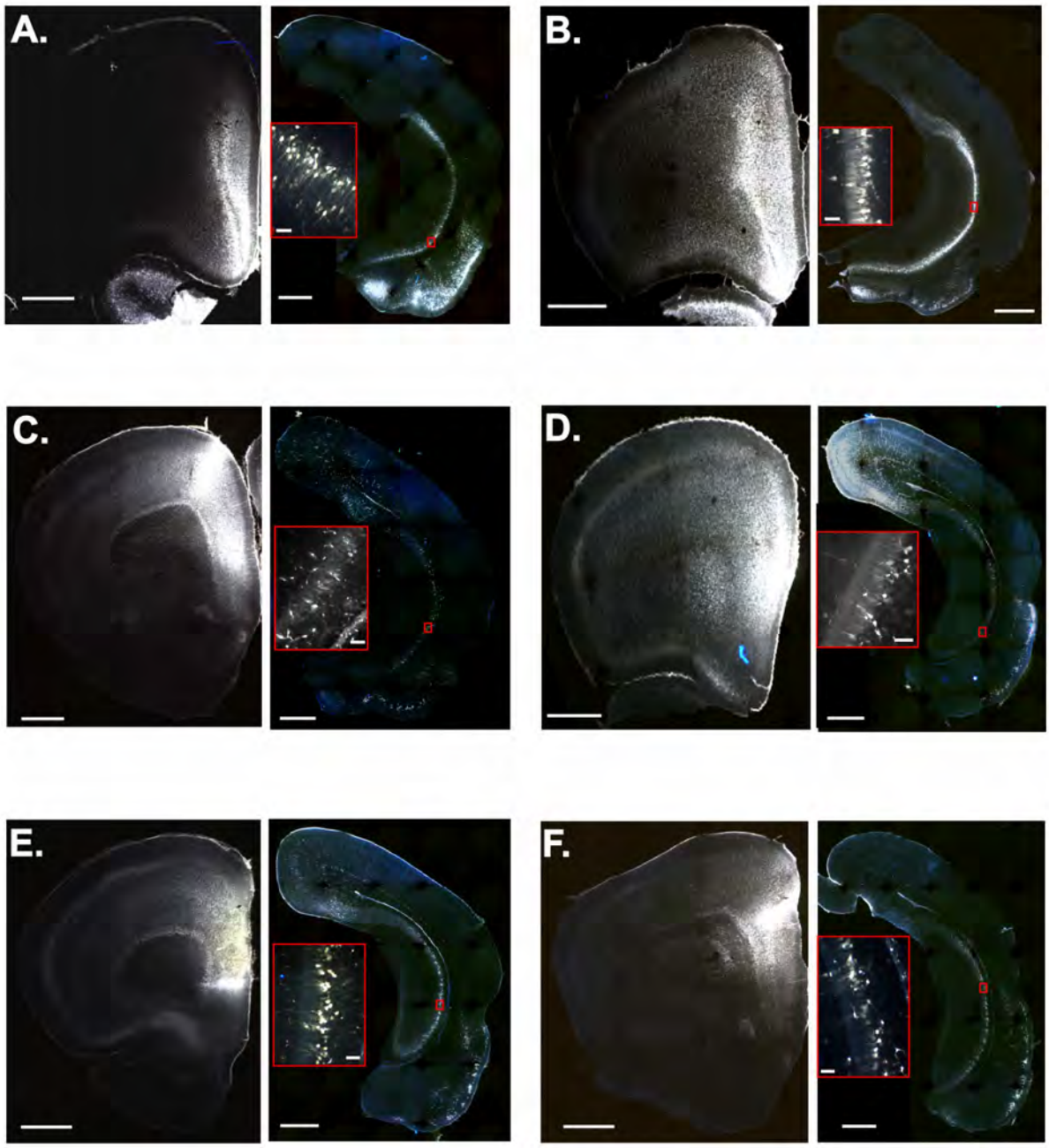

Figure S6. Development of synaptic projections from the Hipp to the PFC. Brightfield photomicrographs displaying retrogradely labeled neurons accumulating in the CA1 area and EC of all investigated P7 rats after FG injection in the PFC at P1 (left). Scale bars correspond to 1 mm. Insets, retrogradely labeled CA1 neurons (red boxes) displayed at higher magnification. Scale bars correspond to 50 µm.

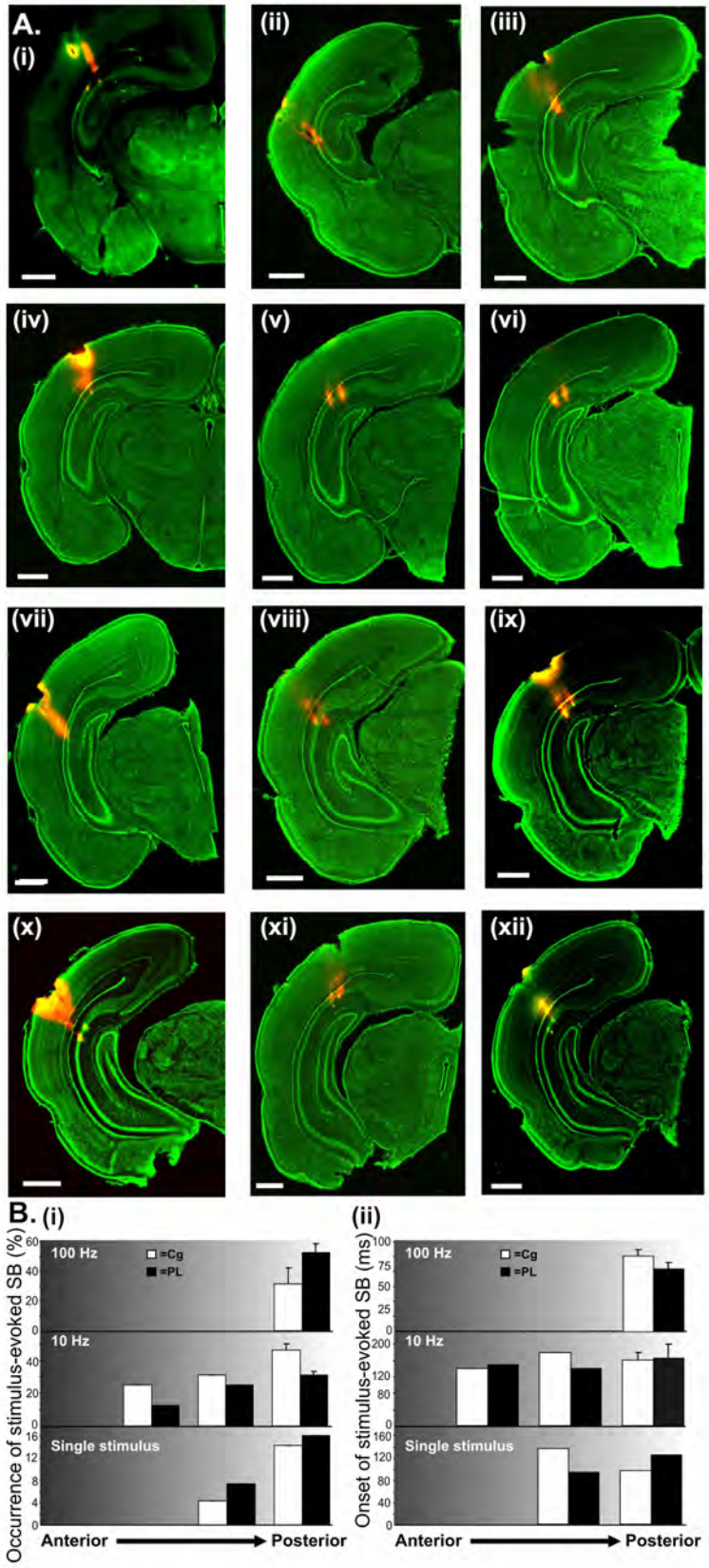

Figure S7. Electrical stimulation of the hippocampal CA1 area. (A) Digital photomontage reconstructing the location of the DiI-labeled bipolar stimulation electrode (orange) in the CA1 region of Nissl-stained 100 µm-thick coronal sections (green) from 12 investigated rats (i-xii). Scale bars correspond to 1 mm. (B) Relationship between the position of the stimulation electrode in the hippocampal CA1 area and the occurrence (i) or onset (ii) of the evoked SB elicited in the Cg (white bars) and PL (black bars) after single or repetitive stimulation. The positions of the stimulation electrode in the intermediate and ventral Hipp of different pups were aligned from anterior to posterior and grouped. The occurrence was normalized to the total number of stimulations (100%).

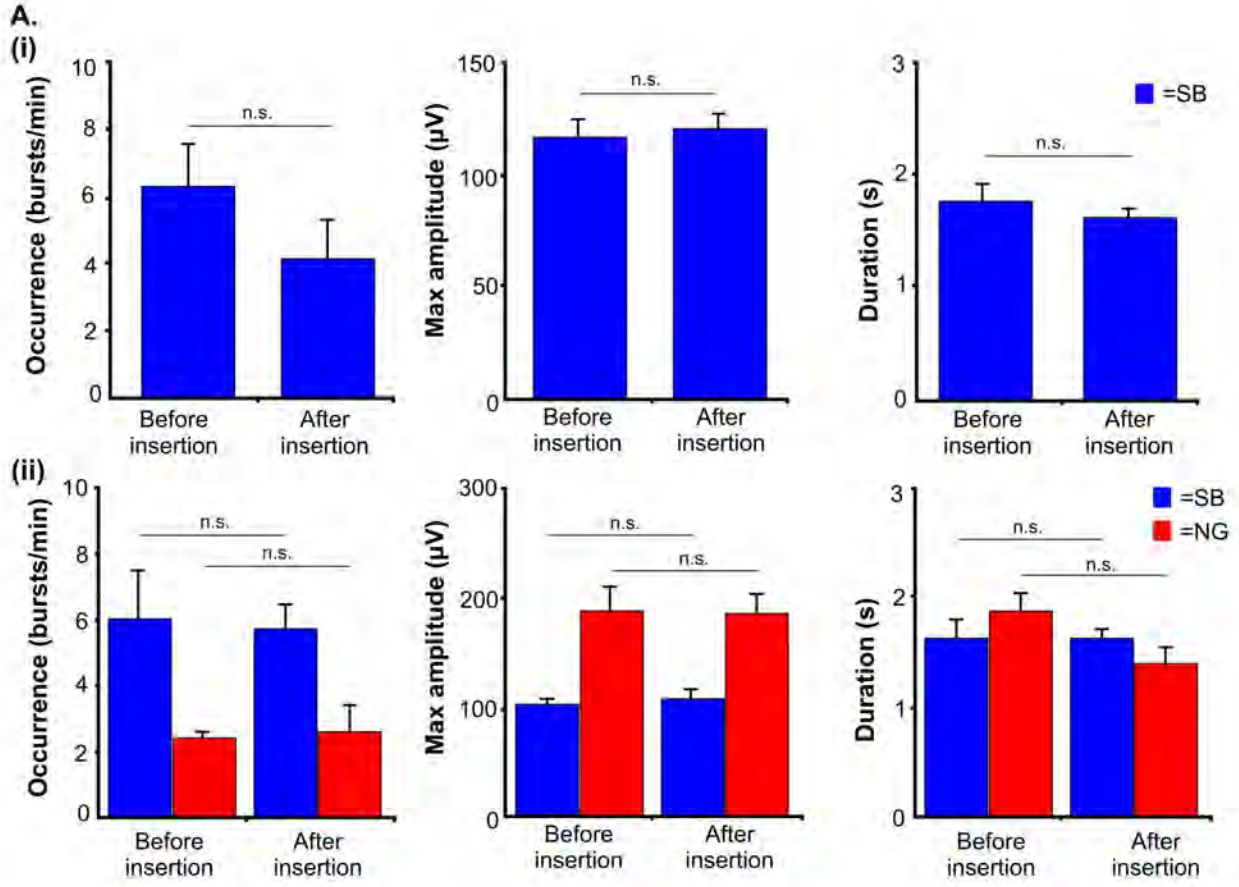

Figure S8. Properties of prefrontal oscillations elicited by electrical stimulation of the intermediate Hipp. (A) Effects of insertion of the stimulation electrode into the Hipp on the prefrontal SB and NG recorded from 3 rats. (i) Bar diagrams displaying the similar occurrence (left), amplitude (middle) and duration (right) of SB in the Cg before and after the insertion of the bipolar stimulation electrode. The low number of NG spontaneously occurring in the Cg precluded their statistical analysis. (ii) Same as (i) for the prelimbic SB (blue) and NG (red). Data are displayed as mean ± SEM.

Total number	P0	P1	P2	P3	P4	P5	P6	P7	P8	P9	P10	P11	P12	P13	P14
213	6	9	7	5	4	11	16	65	18	22	6	7	6	16	15
Exp. Aims				**Characterization of the prefrontal activity**				**Characterization of the hippocampal activity**				**Characterization of the prefrontal-hippocampal interactions**			
Number of investigated pups				104				33				106			

Table S1. Distribution of the total number of investigated pups over the first 15 postnatal days (P) and over different experimental aims. Some pups were used for more than one aim.

Properties	SB		NG	
	Cg	PL	Cg	PL
Occurrence (bursts/min)	1.45 ± 0.09 ***	0.89 ± 0.05	0.29 ± 0.04	1.03 ± 0.06 ***
Amplitude (μV)	119.43 ± 1.58	121.09 ± 2.26	201.75 ± 5.39	258.36 ± 3.88 ***
Duration (s)	1.98 ± 0.03 ***	1.68 ± 0.03	2.24 ± 0.08	2.01 ± 0.04
Main frequency (Hz)	7.59 ± 0.06	7.78 ± 0.1 ***	8.93 ± 0.25	9.11 ± 0.15
Delta relative power (%)	4.73 ± 0.07	4.86 ± 0.1	2.89 ± 0.13	3.06 ± 0.09
Theta relative power (%)	38.96 ± 0.31	38.95 ± 0.43	32.82 ± 0.95	31.96 ± 0.49
Alpha relative power (%)	24.28 ± 0.21 ***	20.6 ± 0.25	22.71 ± 0.57	21.35 ± 0.33
Beta relative power (%)	23.71 ± 0.29	25.77± 0.45	31.81 ± 0.94	33.2 ± 0.5 ***
Gamma relative power (%)	8.29 ± 0.11	9.79±0.15 ***	9.76 ± 0.41	10.42 ± 0.26
Absolute power ($x10^8$ μV^2/Hz)	2.29 ± 0.000001 *	1.66 ± 0.000002	6.11 ± 0.000005	8.14 ± 0.000006 *

Table S2. Properties of SB and NG in the Cg vs. PL. Values were averaged for all recording sites located within the Cg and PL. Mann-Whitney test was used and significance values ($p<0.05$, *; $p<0.01$, **, $p<0.001$, ***) are marked for the area with the highest value.

Age group	*Properties*	*Sharp waves (SPWs)*	*Theta oscillations with SPWs*	*Theta oscillations w/o SPWs*	*Gamma oscillations*	*Ripples*
Intermittent activity (P0-9)	Onset (postnatal day)	0	1	1	7	7
	Occurrence (events/min)	4.24 ± 0.65	1.35 ± 0.30	2.55 ± 0.48	-	0.31 ± 0.03[§]
	Amplitude (μV)	90.78 ± 3.50	80.18 ± 3.25	52.24 ± 1.91	-	
	Duration (s)	0.08 ± 0.002	3.83 ± 0.26	2.44 ± 0.12	-	0.022 ± 0.001
	Dominant frequency (Hz)	-	6.85 ± 0.12	7.11 ± 0.21	36.38 ± 0.44	139.21 ± 3.33
Continuous activity (P10-15)	Occurrence (events/min)	-	-		-	0.83 ± 0.13[§]
	Amplitude (μV)	192.88 ± 10.50	261.07 ± 8.67		-	-
	Duration (s)	0.06 ± 0.002	-		-	0.048 ± 0.009
	Dominant frequency (Hz)	-	6.68 ± 1.16		34.43 ± 0.28	128.64 ± 4.28

Table S3. Properties of the activity patterns in the CA1 area of the intermediate hippocampus during postnatal development.
[§]The occurrence of ripples was calculated as fraction of SPWs with ripples from the total number of SPWs.

Supplemental Experimental Procedures

Surgical preparation

All experiments were performed in compliance with the German laws and the guidelines of the European Community for the use of animals in research and were approved by the local ethical committee. Pregnant Wistar rats were obtained at 14-17 days of gestation from the animal facility of the University Medical Center Hamburg-Eppendorf, housed individually in breeding cages with a 12 h light/12 h dark cycle and fed ad libitum. Extracellular recordings were performed in the PFC (2-2.5 mm anterior to bregma and 0.2-0.7 mm from the midline) and intermediate Hipp (3-5 mm posterior to bregma and 3-5 mm from the midline) of P0-14 male rats and in the S1 (1-3 mm posterior to bregma, 2-3.5 mm from the midline) and V1 (0.5-1 mm anterior to lambda and 2-3 mm from the midline) of P0-3 male rats using experimental protocols as described previously (Hanganu et al., 2006; Yang et al., 2009). Under light urethane-anesthesia (0.125-1g/kg; Sigma-Aldrich), the head of the pup was fixed into the stereotaxic apparatus (Stoelting, Wood Dale, IL) using two metal bars fixed with dental cement on the nasal and occipital bones, respectively. The bone over the PFC and Hipp was carefully removed by drilling holes of less than 0.5 mm in diameter. Removal of the underlying dura mater by drilling was avoided, since leakage of cerebrospinal fluid or blood damps the cortical activity and single neuronal firing (I. Hanganu-Opatz, personal observations). The body of the animals was surrounded by cotton and kept at a constant temperature of 37 °C by placing it on a heating blanket. During recordings, urethane anesthesia (0.1-0.2 times the initial dose) was given when the pups showed any sign of distress (n=2 out of 213 pups). After a 20-60 min recovery period, multitetrodes or multielectrode arrays (Silicon Michigan probes, NeuroNexus Technologies) were inserted perpendicularly to the skull surface into the PFC until a depth of 3 mm, perpendicularly or at 20° from the vertical plane into Hipp at a depth of 2.5-3.5 mm, and perpendicularly into the S1 or V1 until a depth of 1.5 mm. The electrodes were labeled with DiI (1,1'-dioctadecyl-3,3,3',3'-tetramethyl indocarbocyanine, Invitrogen) to enable post-mortem in histological sections the reconstruction of electrode tracks in the PFC and Hipp (Fig 1A, Fig. S3A). One or two silver wires were inserted into the cerebellum and served as ground and reference electrodes. Miniature earphones placed under the pup's body were sensitive enough to detect the smallest visible movements of the limbs as well as the breathing of pups during recordings.

Recording and stimulation protocols

Simultaneous recordings of FP and MUA were performed from the PFC and Hipp using one-shank and four-shank 8- or 16-channel Michigan electrodes (0.5-3 MΩ) as well as multitetrodes (0.5-1.1 MΩ). The recording sites were separated by 100 or 200 µm in vertical direction for one-shank electrode, by 50 µm in vertical and by 125 µm in horizontal direction

for the four-shank electrode, and by 25 µm for the multitetrodes. The recording sites covered the prefrontal sub-divisions Cg and PL (Van Eden and Uylings, 1985) and the CA1 area in the intermediate Hipp. Both FP and MUA were recorded for at least 900 s at a sampling rate of 32 or 25 kHz using a multi-channel extracellular amplifier (Digital Lynx 4S with no gain, Neuralynx, Bozeman, MO or USB-ME16-FAI-System with gain of 1000, Multichannel Systems, Reutlingen, Germany) and the corresponding acquisition software (Cheetah or MC-RACK). During recording the signal was band-pass filtered between 0.1 Hz and 5 kHz (Digital Lynx) and 1 Hz and 5 kHz (MCS). For electrical stimulation of the Hipp, single or trains of electrical pulses (4-7 V, 10 stimuli at 10 or 100 Hz) were applied every 60 s via a bipolar tungsten electrode (4 MΩ, tip separation of 1 mm, FHC, Bowdoinham, ME) inserted into the CA1 area of the Hipp at 1.7-2 mm depth. Only oscillations that started within the first 300 ms after stimulus were considered as evoked events. The exact position of the stimulation electrode was reconstructed post-mortem in all investigated pups by tracing the tracks of DiI-labeled stimulation electrodes (Fig. S7).

Impairment of hippocampal activity

Acute and reversible impairment of hippocampal activity was induced by injection of lidocaine (Sigma-Aldrich, 1% in 0.9% saline, pH 7.0 with NaOH, 10-20 nl, 10 nl/min) into MS (+0.2 mm anterior to bregma, 0.1 mm from the midline, 4-5 mm depth) of P6-8 male rats. For chronic impairment of hippocampal drive to PFC, either excitotoxic lesion of intermediate/ventral, but not dorsal Hipp using NMDA (Sigma-Aldrich) or selective lesion of septal GABAergic neurons using GAT1-SAP (Advanced Targeting Systems, San Diego, CA) was induced. Male P0-1 rats from litters of 8 to 12 pups including both male and female pups were used. A constant ratio male:female (between 3:1 and 3:2) was kept within litters, since early behavior of rat pups depends on sex structure of the litter (Brain and Griffin, 1970). The previously described surgery protocol (Lipska and Weinberger, 1993) was modified for newborn rats. Anesthetized pups were immobilized by taping onto a preformed mold fixed into a stereotaxic apparatus. The skin overlaying the skull was incised. A 26GA needle attached to a 10 µl-microsyringe pump controller (Micro 4, World Precision Instruments, Sarasota, FL) was used to inject, at slow rate (10-20 nl/min), a total amount of 20-50 nl NMDA (40 mM in 0.1 M phosphatase-buffered saline (PBS) pH 7.4) or vehicle (0.1 M PBS, pH 7.4) into intermediate/ventral Hipp or 20-40 nl GAT1-SAP (325 ng/µl in artificial cerebrospinal fluid, ACSF) or vehicle (ACSF) into the MS. Both lidocaine and GAT1-SAP injected into the MS acted on a small radius of ~200 µm (Tehovnik and Sommer, 1997) confined to the septal area. Single injections were performed on one or both hemispheres. The small size and the fragility of the pup's skull immediately after birth precluded NMDA injections at multiple sites that would have ensured a better distribution over hippocampal areas (Jarrard, 1989). After injection, the needle was left in place for additional 4 min to allow optimal diffusion of the

solution and prevent the backflow of injected fluid along the syringe track. The scalp wound was closed with tissue adhesive. Two pups with seizures after NMDA-injection were excluded from the analysis. Pups were returned to the dam only after a full recovery of body temperature and motility (30-60 min) to prevent maternal cannibalism. In each investigated litter non-treated, PBS- or ACSF- and NMDA- or GAT1-SAP-treated pups were investigated daily (weight, reflexes, and developmental milestones). At P7-8, the pups were anesthetized, fixed in the stereotaxic apparatus as described above, and investigated for their prefrontal patterns of activity.

Retrograde tracing and staining protocols

Male Wistar rats received at P1 or P6 bilateral injections of Fluoro-Gold (FG, Fluorochrome). A total volume of 0.2-0.5 µl FG (5% in distilled water) was delivered via a 26GA needle attached to a 10 µl-microsyringe pump controller into the PFC. The slow injection speed (0.1 µl/min) and the maintenance of the syringe in place for at least 2-3 min ensured an optimal diffusion of the tracer. After a survival time of 6-13 days the rats were deeply anesthetized with 10% ketamine (aniMedica, Senden-Bösensell, Germany) and 2% xylazine (WDT, Garbsen, Germany) in NaCl (10 µl/g body weight, i.p.) and perfused transcardially with 4% paraformaldehyde (PFA) dissolved in 0.1 M phosphate buffer, pH 7.4. The brains were removed and postfixed in the same solution for 24 h. Blocks of tissue containing the PFC and the Hipp were sectioned in the coronal plane at 40 µm. The sections were air dried, coverslipped with DPX (Sigma-Aldrich) and examined using an ultraviolet excitation filter of a Zeiss Imager M1 microscope. The photographs were adjusted for brightness and contrast using Corel PhotoPaint 12.

Parvalbumin (PV) immunoreactivity was revealed according to previously reported protocols (Pang et al., 2010). Briefly, deeply anaesthetized rats were perfused transcardially with PFA and the overnight postfixed brains were sectioned in the coronal plane at 50 µm and stored in PBS. The sections including the MS were preincubated for 2 h with PBS-containing 2% normal horse serum, 1% albumin from bovine serum and 0.2% Triton X-100 to block unspecific staining. Incubation with rabbit anti-PV IgG (1:1000, Svant, Bellinzona, Switzerland) for 3 days was followed by incubation with the secondary antibody Alexa Fluor donkey anti-rabbit IgG for 1.5 h. Sections were rinsed in PBS, air-dried, and coverslipped with Fluoromont (Biozol, Eching, Germany). The immunoreactivity was examined using the red (568 nm) excitation filter of the fluorescence microscope. The photographs were adjusted for brightness and contrast using Corel Photopaint. The stained cells in the MS [as identified according to Ashwell and Paxinos (2008)] were counted and their density (stained cells per mm^2) calculated.

Fluorescent Nissl staining was performed as previously described (Quinn et al., 1995) using the NeuroTrace® 500/525 green fluorescent Nissl stain (Invitrogen). Briefly, rehydrated slices

were incubated for 20 min with 1:100 diluted NeuroTrace. Sections were washed, coverslipped with Fluoromount and examined using the green filter (AF 488). Series of coronal sections (100 µm) were collected for documenting the size of the hippocampal lesion after NMDA injection. Size and coordinates of lesion were reconstructed for each subject using ITEM software (Soft Imaging Systems, Münster, Germany).

Data Analysis

Characterization of neonatal and pre-juvenile patterns of oscillatory activity. To detect the oscillatory events, the raw data were filtered between 4-80 Hz or between 100-300 Hz using a Butterworth three-order filter. Discontinuous or continuous slow oscillations in theta-alpha frequency band were detected as FP deflections exceeding five times the baseline SD. Only discontinuous slow events lasting >100 ms, containing at least three cycles, and being not correlated with movement (twitches) were considered for analysis. For continuous activity movement-associated epochs were removed. Fast events (gamma episodes, gamma oscillations, ripples) superimposed on slow events were detected either automatically or by eye and confirmed by time-frequency plots. SB were classified according to previously described criteria (Khazipov et al., 2004; Hanganu et al., 2006). The presence of short gamma episodes automatically detected after 30-100 Hz filtering and confirmed by eye on at least one third of the cycles in intermittent slow oscillations led to classification of these events as NG. Intermittent oscillatory events, SB and NG in the PFC as well as theta bursts in the hippocampal CA1 area, were analyzed in their occurrence (defined as the number of bursts per min), duration, max amplitude (defined as the voltage difference between the maximal positive and negative peaks), dominant frequency as well as absolute and relative power in theta (cortical: 4-8 Hz, hippocampal: 4-10 Hz), alpha (cortical: 8-13 Hz), and beta (cortical: 13-30 Hz) frequency bands. For fast discontinuous oscillations [gamma oscillations (30-80 Hz) and hippocampal ripples (100-300 Hz)] the duration and dominant frequency were investigated. Oscillatory activity was defined and analyzed as continuous if the average interburst interval was below 0.5 s. For continuous oscillatory activity same parameters as for slow intermittent events, except occurrence and duration, were analyzed for 5-15 consecutive 60 s-long time windows. Time-frequency plots were calculated by transforming the FP events using Morlet continuous wavelet. Minimal and maximal intensities in power were normalized to values between 0 and 1 and were displayed in dark blue and red, respectively. For visualization of data "whitened" spectrograms were calculated as previously described (Sirota et al., 2008).

Assessment of correlation between discontinuous or continuous oscillatory patterns at different recordings sites. For this aim several methods were used. In the first instance, the difference between the onset of discontinuous events in the PFC and of hippocampal theta

bursts was calculated. Only prefrontal oscillations starting within 3 s before or after hippocampal bursts were considered for analysis. Prefrontal and hippocampal oscillations were termed simultaneous if their onset difference was <13 ms. Secondly, maximal cross-correlation and coherence coefficients of FP were calculated for all recording sites within PFC by selecting the channel with maximal amplitude as reference and for simultaneously recorded PFC-hippocampal events using the hippocampal signal as reference. As spectral measure of correlation between two signals across frequencies, the coherence was calculated from the cross-spectral density between the two signals and normalized by the power spectral density of each (Jerbi et al., 2007). The computation was performed according to the formula

$$C(f) = \frac{\left|\sum_{i=1}^{N} X_i(f) Y_i^*(f)\right|^2}{\sum_{i=1}^{N} |X_i(f)|^2 \sum_{i=1}^{N} |Y_i(f)|^2},$$

where $X_i(f)$ and $Y_i(f)$ are the Fourier transforms of the signals x and y for the i data segment at frequency f, and * indicates the complex conjugate. The computations were carried out by using the magnitude-squared coherence function (MATLAB) based on Welch's averaged periodogram method (non-overlapping 0.5 s time window, frequency resolution 1 Hz). Within PFC, cross-correlation and coherence values ranging from 0 (events are uncorrelated) to 1 (events are perfectly correlated) were encoded from dark blue (0) to red (1) and displayed in cross-correlation and coherence maps. Within these maps, events were considered as highly synchronized whether their cross-correlation and coherence coefficients were >0.7. Half of cingulate SB (288 out of 576) appeared widely synchronized. One third of them preferentially synchronized the cortical plate (CP) and layers II/III, since the average cross-correlation (0.91 ± 0.01, n=224 bursts from 4 pups) and coherence coefficients (0.96 ± 0.003) at recording sites located in the upper layers were significantly ($p<0.001$) higher than those calculated for the deeper layers and the remnant of the subplate (0.61 ± 0.01, 0.77 ± 0.01, n=224 bursts from 4 pups). The relative low occurrence of NG precluded a consistent analysis of their coupling over the Cg. In the PL, most of SB (720 out of 1200) were also widely synchronized. The majority of prelimbic NG (768 out of 1472) synchronized the upper layers and the CP, since the average cross-correlation and coherence coefficients (0.86 ± 0.005, 0.93 ± 0.004, n=768 bursts from 5 pups) were significantly ($p<0.001$) higher than at recording sites located in the deeper prelimbic layers (0.54 ± 0.008, 0.77 ± 0.008) (Fig. 3D). Local oscillatory events with low occurrence that were restricted to one or two recording sites could be recorded only in the PL, but not in the Cg.

Thirdly, a sliding window procedure was developed to calculate the cross-correlation coefficients for simultaneously recorded oscillations in the PFC and Hipp at specific time points across the entire data segment. Windows of 0.5 s in duration were moved across the

data segment in increments of 0.2 s and their spectral analysis was performed for original and shuffled (oscillations recorded at different time points) data. For intermittent activity shuffling was achieved by randomly selecting oscillatory events of similar duration in the PFC and Hipp, whereas time windows of 50 s lag were used for continuous activity. Cross-correlation values ranging from -1 (anticorrelation) over 0 (no correlation) to 1 (maximal correlation) were color-coded as blue and red, respectively.

Current source density (CSD) analysis. CSD profiles were calculated from the field potential profiles according to a five point formula described by Nicholson and Freeman (Nicholson and Freeman, 1975}. The CSD values $\mathrm{I_m}$ were derived from the second spatial deviation of the extracellular field potentials Φ and calculated by the finite-difference formula

$$\mathrm{I_m} = -(1/kh^2)\sum_{m=-n}^{n} a_m \Phi(X + mh),$$

where h is the distance between successive measuring points (100 µm in the present investigation) and X is the coordinate perpendicular to the cortical layer. The remaining constants are as follows: n = 2, k = 4, a_0 = -2, $a_{\pm1}$ = 0 and $a_{\pm2}$ = 1. In the CSD profiles, current sinks are indicated by downward deflections and sources by upward deflections. To facilitate visualization of CSD profiles, we generated color image plots by linear interpolation along the depth axis. The blue color represented current sinks and red color represented current sources.

Spectral analysis and Granger causality. The analysis of directed interactions between simultaneously recorded prefrontal and hippocampal activity was based on the concepts of Wiener-Granger causality (Granger, 1969; Geweke, 1982) applied to autoregressive (AR) models of the data. Statistically, for two simultaneously measured time series, one series can be defined as causal to the other if the second series can be better predicted by incorporating past knowledge from the first one. If the prediction error for the second time series at the present time is reduced by including past data from the first time series in the linear regression model, then the first series can be defined as having a causal or driving influence on the second time series. The previously described analysis (Ding et al., 2006; Bollimunta et al., 2008) and the corresponding toolbox BSMART (Cui et al., 2008) were modified to fit long single trial data that are not event-related and were divided in short segments of 1 s. Briefly, each pair of signals at time t were denoted by $\mathbf{X}_t = (x_{1t}, x_{2t})^{\mathrm{T}}$, where T represent the matrix transposition. Considering that the data can be described by the following AR model:

$$\sum_{k=0}^{m} A_k X_{t-k} = E_t,$$

where $\mathbf{E}_t$ is a temporally uncorrelated residual error series with covariance matrix Σ, and $\mathbf{A}_k$ are 2 x 2 coefficient matrices to be estimated from the data, we determined the model order *m* by the Akaike information criterion (Akaike, 1974). For all data *m*=14 was chosen to have optimal spectral resolution and a minimum of overparamerization. Under these conditions the spectral matrix can be evaluated as

$$S(f) = H(f)\sum H^*(f)$$

where the asterisk denotes matrix transposition and complex conjugation, and

$$H(f) = (\sum_{k=0}^{m} A_k e^{-2\pi i k f})^{-1}$$

is the transfer function. The power spectrum of channel *I*, which is either 1 or 2 is given by $S_{II}(f)$. The Granger causality spectrum from x_{2t} to x_{1t} is defined as shown previously (Brovelli et al., 2004; Ding et al., 2006; Anderson et al., 2010)

$$I_{2\to 1}(f) = -\ln(1 - \frac{(\sum_{22} - \frac{\sum_{12}^2}{\sum_{11}})|H_{12}(f)|^2}{S_{11}(f)}),$$

which can be interpreted as the proportion of x'_{2t} causal contribution to the power of the x_{1t} series at the frequency *f* (in this study theta band). Reciprocally, the causality spectrum from x_{1t} to x_{2t} can be obtained by switching the indices 1 and 2 in the above equation. Statistical significance for Granger causality was assessed by using the random permutation approach (Brovelli et al., 2004) to build a baseline null-hypothesis distribution. We considered for analysis a large number (between 3000 and 5000) of time segments recorded on two channels in PFC and hippocampus and we assumed that data from different time segments are independent from each other. Consequently, randomly pairing the time segments from one channel with those from the other for a large number of permutations (n=100) produces a distribution of causality spectra corresponding to the null hypothesis.

Spike sorting and analysis. The raw signal was firstly high-pass filtered (>407 Hz). The threshold for detection of multiple unit activity was individually set depending on the geometry of the recording site. As detailed previously (Nicolelis et al., 2003), the stored signals were sorted into similar waveform shapes using the Offline Sorter software (Plexon, Dallas, TX). For depicting the valid waveforms in 2D/3D space a combination of features (including the first three principal components, peak-to-peak voltage amplitudes) was chosen. Shapes of detected waveforms were visually inspected to exclude background noise. A group of similar waveforms was considered as being generated from a single neuron if it defined a discrete cluster in a 2D/3D space and exhibit a refractory period (>1 ms) in the interspike interval (ISI) histograms. Assignment of spikes as being generated by excitatory or inhibitory neurons, as performed in adults is not feasible in neonatal/pre-juvenile

pups due to the absence of reliable differences in spike's shape during development. The quality of separation between identified clusters was assessed by four different statistical measurements: the classical parametric F statistic of multivariate analysis of variance (MANOVA), the J3 and PseudoF (PsF) statistics and the Davies-Bouldin validity index (DB) (Davies and Bouldin, 1979; Spath, 1980). The values of statistical testing ranged between $7.6*10^{-74}$ and 0.75 for MANOVA, 0.13 and 13.78 for J3, 44.03 and 79164 for PsF, and 0.15 and 2.82 for DB.

Bursts of neuronal firing were detected in the spike trains by using the "Rank surprise" statistics, a nonparametric ISI-distribution-free approach based on the ranks of ISI in the entire spike train (Gourevitch and Eggermont, 2007). For each spike train (n=6) the percentage of spikes assembled in bursts (ISI value < 30 ms) was determined. Only spikes that occurred during oscillations were included in the analysis.

Assessment of relationship between network oscillations and neuronal firing. Coupling of slow (theta) and fast (gamma) rhythms of NG as well as of prelimbic nested gamma episodes and MUA/spike discharge were assessed. The Hilbert transform was applied to the raw signal that was band-pass filtered (4-25 Hz and 25-60 Hz, respectively) using a Butterworth filter in forward and reverse direction to avoid phase distortion. Gamma episodes were detected automatically when the power of signal exceeded twice the SD. The cross-correlation between gamma onsets and spike train was calculated for a time lag of 150 ms using a bin size of 2 ms. 99%-confidence intervals were calculated as

$$\overline{\chi} \pm 2.58\frac{\sigma}{\sqrt{n}},$$

where $\overline{\chi}$ is the mean firing rate during NG, σ is the standard deviation and n is the total number of NG events. To characterize the relationship between gamma episodes and phase of NG each NG cycle was divided ·/20-long bins and the occurrence probability of gamma episodes on each of them was calculated by normalizing the sample points within gamma episodes to the total number of sample points.

The phase-locking of spikes with the FP was assessed using a previously described algorithm based on Rayleigh Z-statistic (Siapas et al, 2005; Hangya et al., 2009). If the firing of a neuron is modulated by the theta rhythm of the burst then its phase over the theta cycle is not uniformly distributed. The significance of the unimodal preference was tested by Rayleigh's Z statistics (Siapas et al., 2005). Phases of hippocampal theta bursts and prefrontal gamma episodes were determined using the Hilbert transform (phase of 0 refers to the peak and phase of · refers to the trough of the cycle), and a specific phase was assigned to each spike based on the time of spike's occurrence. The spike trains were converted into a sequence of unit length vectors oriented by the phase values of their corresponding spikes. The orientation of the mean resulting vector was defined as preferred phase. The phase

locking between spikes and FP was tested for significance using the Rayleigh statistic that is defined as $Z=nR^2$, where R denotes the mean resultant length of the given phase series. The probability that the null hypothesis of sample uniformity holds is given by

$$P = e^{-Z}\left[1+(2Z-Z^2)/(4n)-(24Z-132Z^2+76Z^3-9Z^4)/(288n^2)\right]$$

For n > 50, the approximation $P = e^{-Z}$ is adequate (Mardia, 1972; Fisher, 1993; Zar, 1998).

Cross-covariance analysis

The interactions between pairs of simultaneously recorded spike trains were quantified as previously detailed (Siapas et al., 2005) by calculating the cross-covariance for each given cell pair (i,j) according to the function

$$q_{ij}(u)dudt = \mathrm{cov}\left[dN_i(t+u)dN_j(t)\right],$$

where u represents the lag and dN(t) takes values of 0 or 1 depending whether or not a spike occurred in the time interval between t and t+dt (time bin 5 ms). The results were normalized to unit variance by assessing the standardized cross-covariance

$$Q_{ij}(u) = \sqrt{\frac{bT}{P_iP_j}}q_{ij}(u),$$

where b is the bin size, T the period of observation, and P_i, P_j the mean firing rates.

The mean standardized cross-covariance was calculated by summing the Q_{ij} for all cell pairs and dividing it by the square root of the number of pairs. Q_{ij} was subsequently smoothed by 25 ms. Significance for Q_{ij} was calculated for each prefrontal-hippocampal cell pair as previously described (Siapas et al., 2005). Assessment of the significant interactions between cell pairs was hampered by the very low firing rates that can produce spurious significant correlations not attenuated by subsequent averaging.

Assessment of volume conduction. To decide on the presence of conduction synchrony between the PFC and Hipp, the coherence between prefrontal (prelimbic) spikes and hippocampal FP was calculated as previously described (Soteropoulos and Baker, 2006). Briefly, spike trains were converted to a waveform with the same sampling rate as the FP assigning 1 to periods of MUA and 0 to MUA-free windows. Coherence between the resulting binary values and FP was calculated. Only time windows corresponding to intermittent oscillations were used for further coherence analysis. The significance threshold was calculated for original vs. shuffled (randomly distributed spikes before conversion to waveform) data.

Supplemental References

Akaike,H. (1974) A new look at the statistical model identification. IEEE Trans. Auto Contr. *19*, 716-723.

Ashwell, K.W.S., Paxinos, G. (2008) Atlas of the developing rat nervous system. 3rd edition. Elsevier. Academic Press.

Bollimunta,A., Chen,Y., Schroeder,C.E., and Ding,M. (2008). Neuronal mechanisms of cortical alpha oscillations in awake-behaving macaques. Journal of Neuroscience *28*, 9976-9988.

Brain,C.L. and Griffin,G.A. (1970). The influences of the sex of littermates on body weight and behaviour in rat pups. Anim Behav. *18*, 512-516.

Brovelli,A., Ding,M., Ledberg,A., Chen,Y., Nakamura,R., and Bressler, S.L. (2004). Beta oscillations in a large-scale sensorimotor cortical network: directional influences revealed by Granger causality. Proc. Natl. Acad. Sci. U.S.A *101*, 9849-9854.

Cui,J., Xu,L., Bressler,S.L., Ding,M., and Liang,H. (2008). BSMART: a Matlab/C toolbox for analysis of multichannel neural time series. Neural Netw. *21*, 1094-1104.

Davies,D.L., and Bouldin,D.W. (1979). A cluster separation measure. IEEE Pattern Anal. Mach. Intell. *1*, 224–227.

Ding,L., Worrell,G.A., Lagerlund,T.D., and He,B. (2006). Spatio-temporal source localization and Granger causality in ictal source analysis. Conf. Proc. IEEE Eng Med. Biol. Soc. *1*, 3670-3671.

Fisher,N. (1993) Statistical analysis of circular data. (Cambridge: Cambridge University Press).

Geweke,J. (1982). Measurement of linear-dependence and feedback between multiple time-series. J. Am. Stat. Assoc. *77*, 304-313.

Granger,C.W.J. (1969). Investigating causal relations by econometric models and cross-spectral methods. Econometrics *37*, 424-438.

Jarrard,L.E. (1989). On the use of ibotenic acid to lesion selectively different components of the hippocampal formation. Journal of Neuroscience Methods *29*, 251-259.

Lipska,B.K. and Weinberger,D.R. (1993). Delayed effects of neonatal hippocampal damage on haloperidol-induced catalepsy and apomorphine-induced stereotypic behaviors in the rat. Brain Res.Dev.Brain Res. *75*, 213-222.

Mardia,K. (1972). Statistics of directional data. (New York: Academic Press).

Nicholson,C. and Freeman,J.A. (1975). Theory of current source-density analysis and determination of conductivity tensor for anuran cerebellum. J. Neurophysiol. *38*, 356-368.

Nicolelis,M.A., Dimitrov,D., Carmena,J.M., Crist,R., Lehew,G., Kralik,J.D., and Wise,S.P. (2003). Chronic, multisite, multielectrode recordings in macaque monkeys. Proc Natl Acad Sci U S A *100*, 11041-11046.

Quinn,B., Toga,A.W., Motamed,S., and Merlic,C.A. (1995). Fluoro nissl green: a novel fluorescent counterstain for neuroanatomy. Neuroscience Letters *184*, 169-172.

Spath,H. (1980). Cluster analysis algorithms. Ellis Horwood, Chichester, England.

Tehovnik,E.J., and Sommer,M.A. (1997). Effective spread and timecourse of neural inactivation caused by lidocaine injection in monkey cerebral cortex. J Neurosci Methods. *74*, 17-26.

Zar,J. (1998) Biostatistical analysis. 4th edition. (Upper Sadle River NJ. Prentice Hall).